

The highly tunable Mg-Ni-H switchable mirror system

J.L.M. van Mechelen^{1,*}

¹*Faculty of Sciences, Department of Physics and Astronomy, Condensed Matter Physics,
Vrije Universiteit, De Boelelaan 1081, 1081 HV Amsterdam, The Netherlands*

The Mg-Ni-H switchable mirror system shows a spectacular composition dependence in the hydrogenated state. The optical transmission of a hydrogenated Mg-Ni-H gradient film displays a stripe-like pattern that consists of alternating regions of high and low transmission. This behavior is peculiar as the composite Mg-Ni-H phase diagram only predicts a gradual change between MgH_2 and Mg_2NiH_4 which can not account for the observed composition dependence. In order to understand the observed transmission pattern, the Mg-Ni-H system has been investigated optically, electrically, structurally and morphologically in the metallic and hydrogenated state. As-deposited, metallic, Mg-Ni composition gradient thin films contain the Mg_2Ni and MgNi_2 phases for well-defined composition regions. In the hydrogenated state, vibrational spectroscopy shows the composition dependence of semiconducting Mg_2NiH_4 which is formed from metallic Mg_2Ni . On exposure to hydrogen, physical properties change as well near the equiatomic composition and the composition of MgNi_2 , pointing to possible hydride formation. The strong composition dependence of the Mg-Ni-H system, expressed in the observed transmission, can eventually be understood from the distribution of Mg_2NiH_4 and the occurrence of MgH_2 for higher Mg contents.

I. INTRODUCTION

In 1996 Huiberts *et al.*¹ discovered the dazzling optical changes of yttrium and lanthanum upon the absorption of hydrogen. On exposure to hydrogen, a switchable mirror thin film changes from reflecting to transparent while undergoing a metal-to-insulator transition. All rare earth and Mg alloyed rare earth metal hydrides² possess these properties. In 2001, Richardson *et al.*³ found that alloys composed of Mg and transition metals like Ni, Co, Fe and Mn also switch reversibly. Among these rare earth free metal hydrides, Mg_2NiH_4 received special attention because of its hydrogen storage capacity with an improved kinetics compared to MgH_2 and because of its possible application as smart coating⁴.

In the metallic Mg-Ni system, the Mg-Ni bulk phase diagram shows that Mg_2Ni and MgNi_2 are the two existing intermetallic phases at room temperature.⁵ Mg_2Ni can absorb hydrogen, whereas it has not been reported for MgNi_2 . During hydrogenation, the metal solid solution $\text{Mg}_2\text{NiH}_{0.3}$ is first formed. On increasing the hydrogen content, the host metal atoms rearrange and a complex hydride structure Mg_2NiH_4 is created that consists of $[\text{NiH}_4]^{4-}$ complexes that are ionically bound to Mg^{2+} . Compared to Mg_2Ni , the stoichiometric Mg_2NiH_4 structure has been expanded by 32 vol.%.⁶ For $T > 510$ K, Mg_2NiH_4 has a cubic structure which becomes monocrinally distorted below this temperature.

For the hydrogenated Mg-Ni-H system, the ternary bulk Mg-Ni-H phase diagram has been calculated thermodynamically from experimental data of the binary constituent systems Mg-H, Ni-H, and Mg-Ni.⁷ The predicted phase diagram shows that the only hydrides that can be formed are Mg_2NiH_4 and MgH_2 . Fig. 1a displays a linearized representation of this phase diagram, where metal inclusions like Mg_2Ni , MgNi_2 , $\text{Mg}_2\text{NiH}_{0.3}$ and Ni are present next to the two hydrides. This corresponds to a non-complete hydrogen loading as observed in prac-

tice⁸. At Mg-rich compositions, the physical properties are dominated by MgH_2 which for decreasing Mg contents is *gradually* replaced by Mg_2NiH_4 . The depicted colors are based on the fact that $\text{Mg}_{0.9}\text{Ni}_{0.1}\text{H}_x$ has a yellow visual appearance,³ Mg_2NiH_4 is red⁹ and MgNi_2 does not react with hydrogen and thus remains a non-transparent metal which is imaged as black.

In order to study composition dependent systems, it is desirable to monitor a continuous range of compositions at the same time. This can be achieved by making thin film samples with a composition gradient for which the element ratio is a monotonic function of the position on the sample. In this way, Mg-Ni composition gradient samples are deposited from the elements. Fig. 1b shows the optical transmission of a Mg-Ni-H composition gradient sample capped with 5 nm Pd on a glass substrate. The sample is hydrogenated in an optical gas loading cell at 50 °C and $p_{\text{H}_2} = 2 \cdot 10^5$ Pa. The composition y of $\text{Mg}_y\text{Ni}_{1-y}$ changes from left to right from 0.85 to 0.55, respectively. When illuminated with white light, a strongly composition dependent stripe-like pattern perpendicular to the gradient becomes visible in transmission. Regions of high transmission alternate with zones of low transmission, while the color mainly changes from brilliant yellow at the Mg rich part to reddish black at the Mg poor side. On the basis of the predicted Mg-Ni-H phase diagram, which indicates only a gradual change between MgH_2 and Mg_2NiH_4 in this composition range, it is impossible to explain the observed composition dependence.

Although the predicted Mg-Ni-H phase diagram can not account for the observed transmission behavior, several physical properties correlate very well. An example is the optical phonon strength of the $[\text{NiH}_4]^{4-}$ cluster of Mg_2NiH_4 displayed as a function of composition (Fig. 1c). The phonon strength is a direct measure for the amount of formed Mg_2NiH_4 and so for the level of transmission due to Mg_2NiH_4 . Comparison with the optical transmission shows the excellent resemblance be-

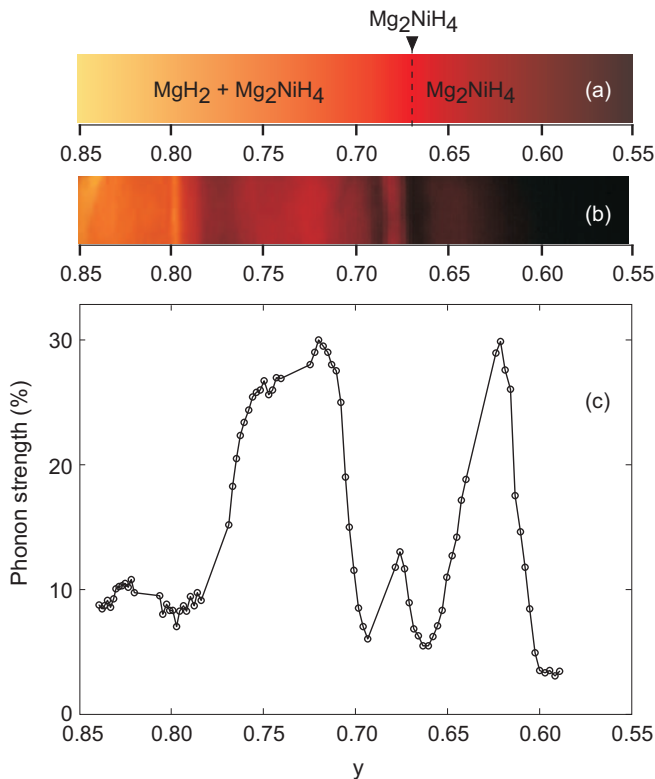


FIG. 1: Illustration showing the inconsistency between (a) the predicted (linearized) Mg-Ni-H phase diagram as a function of composition y of $\text{Mg}_y\text{Ni}_{1-y}\text{H}_x$ and (b) the camera recorded visible transmission of a hydrogenated Mg-Ni-H gradient thin film, and on the other hand the excellent correlation of the transmission (b) with (c) the phonon strength of the $[\text{NiH}_4]^{4-}$ cluster, indicating the amount of formed Mg_2NiH_4 and therefore the level of optical transmission due to Mg_2NiH_4 .

tween both properties for compositions $y \lesssim 0.8$.

In summary, the intriguing Mg-Ni-H system does not behave following the predicted Mg-Ni-H phase diagram, but many of its physical properties correlate in a way possible to draw a picture about it. In order to understand the hydrogenated system, first the as-deposited Mg-Ni system is optically, electrically, structurally and morphologically investigated, as reported in section III. Similarities and correlations between the many metallic properties clearly show the presence of site-ordered and structurally disordered intermetallic phases in well-defined composition ranges. Then, section IV reports about the hydrogenated Mg-Ni-H system. The observed stripe-like pattern in transmission is quantified by photometric spectrometry in order to compare it to other optical, electrical and structural phenomena. Correlations between these properties show the stripe-like pattern to be due to a peculiar spatial distribution of MgH_2 and Mg_2NiH_4 together with an enhanced presence of $\text{Mg}_2\text{NiH}_{0.3}$ at certain compositions. Eventually, the influence of hydrogen on the intermetallic phases is demon-

strated by the DC resistivity in the framework of an effective medium theory (Bruggeman approximation) and classical percolation theory.

II. EXPERIMENTAL

A. Film deposition

Mg-Ni films with a compositional gradient are deposited by magnetron co-sputtering in a high-vacuum chamber (base pressure $\sim 10^{-6}$ Pa) at room temperature. The mutual power of the Mg and Ni particle current and their direction with respect to the substrate control the composition regime of the film. As a consequence of the technique, films possess a thickness gradient, which is measured *ex situ* with a Dektak stylus profilometer. Typically, the gradient is almost linear and varies from 300 to 600 nm, increasing towards the Mg rich side. To catalyze the hydrogen uptake and to protect the film from oxidation a homogeneous 4 nm thin Pd cap layer is deposited *in situ* on top of the Mg-Ni film. Mg-Ni gradient films are either deposited on a 70 mm long substrate made of one piece or on seven 10 mm long substrates that are placed next to each other.

B. Composition determination

The composition of as-deposited gradient samples is determined *ex situ* by Wavelength Dispersive X-ray Spectrometry (WDS) and Rutherford Backscattering Spectrometry (RBS). WDS has been carried out in a JEOL JXA-8800M Electron Microprobe. Here characteristic X-rays are produced by the interaction of a $10 \mu\text{m}$ electron beam with the film layer. In order to have the excitation volume mainly within the thin film layer, the acceleration voltage of the beam is adjusted to the thickness and the density of the layer. In this way, the microprobe was operated at 5 kV and 15 kV which allowed the detection of the K_α line of Mg and the L_α and K_α line of Ni, respectively. In order to diminish the background radiation glassy carbon substrates are used, which low energy X-rays can not detect. Most samples for composition analysis did not have the highly absorbing Pd cap layer.

For RBS, $^4\text{He}^+$ ions with an energy of 2 MeV bombard the sample and the energy distribution of the backscattered particles within a solid angle $d\Omega$ is detected. The maximum energy of the scattered ions determines the mass of the scattering centers, from which the present elements and their amounts can be established. In order to diminish the background radiation, also for RBS glassy carbon substrates are used.

WDS makes use of predefined calibration standards and has to apply a matrix correction after the measurement whereas RBS directly measures the backscattered radiation of atomic fractions. On the other hand, the

electron beam size of WDS enables the detection of composition irregularities on a very small scale, while for RBS the diameter of the α particle beam is about 1 – 2 mm. Besides the Mg and Ni amount, RBS analysis also provides the oxygen content of the sample.

For $\text{Mg}_y\text{Ni}_{1-y}$ compositions with $y < 0.83$ WDS and RBS agree within 5%, but the deviation increases at higher Mg contents. Further, in the direction of the composition gradient, WDS showed composition deviations with respect to the gradual composition change on a 250 μm scale, to vary from 0.0067 at $y = 0.86$ to 0.0029 at $y = 0.29$. This indicates a very smooth composition change which is mainly determined by the composition gradient on purpose.

C. Optical measurements

Optical reflection and transmission measurements are performed in two overlapping energy ranges using two Bruker IFS66 Fourier transform infrared spectrometers. The first range extends from 0.72 to 3.5 eV (i.e., 1722 – 354 nm) and covers the visible and near infrared, the second range is between 62 meV and 1.2 eV (i.e., 20 – 1.0 μm) which covers the near, middle and beginning of the far infrared. Hydrogen loading is performed *in situ* in an optical gas loading cell. As the cell could only accommodate 10 mm long samples, seven similar hydrogen loadings were required to obtain information about one long gradient sample. During loading the temperature is below 50 °C and the hydrogen pressure is increased from 10^2 Pa to 2×10^5 Pa. Simultaneously, the mean electrical resistivity over the present composition gradient has been monitored. As the visible and infrared beam diameter at the sample is about 3 mm, optical properties are averaged over only a narrow composition range. Therefore, the reflection in the as-deposited state and the reflection and transmission in the final state could be measured through making line scans perpendicular to the composition gradient.

D. Electrical measurements

The electrical resistivity has been measured in a home-made apparatus which enabled resistivity measurements on gradient samples. The apparatus has a transparent Perspex arm on which four gold, spring damped needles with a tip diameter of 25 μm are mounted in a 2×2 mm² square. On one side, an axis pierces into the arm along which the arm can slide perpendicular to the composition gradient of the sample and around which it can rotate to place the needles on the sample. The gradient sample has zones of 2.5 mm that are electrically isolated by stripes of 0.5 mm which are shadowed during deposition. The empty stripes are necessary to confine the current to the desired composition range. In this way the electrical resistivity has been measured by the Van

der Pauw method¹⁰ which eliminates the additional resistance coming from objects on the electrical path different than the film.

Resistivity measurements of as-deposited gradient samples are carried out *ex situ*. As resistivity changes enormously during the first part of the hydrogen desorption, measurements on hydrided gradient samples are performed in a glove box which contained a mixture of nitrogen and hydrogen.

E. Structural measurements

X-ray diffraction measurements on as-deposited and hydrogenated gradient samples are performed in $\theta - 2\theta$ geometry using a Bruker D8 Discover X-ray diffractometer. Line scans perpendicular to the composition gradient are carried out with a scan time of 60 s per $\delta 2\theta = 0.01^\circ$ using a 5 – 6 mm Cu K_α beam of mean wavelength $\lambda = 1.5418$ Å. A hydrogen filled gas cell, consisting of a partially X-ray transparent beryllium dome, prevented the pre-hydrogenated sample from unloading.

F. Surface morphology

The surface structure has been determined using a JEOL JSM-6301F Scanning Electron Microscope (SEM) and a NanoScope III Atomic Force Microscope (AFM). The SEM operated at an acceleration voltage of 4 kV. The AFM measured in tapping mode using silicon cantilevers. The surface of an as-deposited 70 mm long gradient sample has first been surveyed at a magnification of 40,000 times by SEM. In order to quantify morphology parameters like the surface roughness and the grain size, identical composition regions are measured by AFM.

III. THE Mg-Ni BINARY ALLOY SYSTEM

In this section we will consider the metallic Mg-Ni system, forming the basis of the hydrogenated Mg-Ni-H system. For this purpose as-deposited composition gradient samples are investigated at room temperature. Optical, electrical and structural properties indicate the presence of intermetallic phases and their arrangement in the crystal lattice. Structural probes further describe the interior of the metallic film. Finally, the surface morphology of the metallic layer illustrates the presence of intermetallic phase formation and complements the structural picture.

A. Optical properties

In order to determine the presence of possibly formed phases in as-deposited Mg-Ni composition gradient thin films, optical reflection measurements were performed for

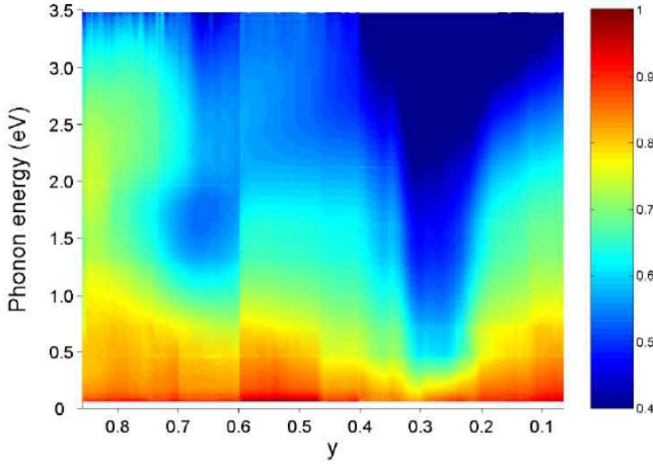


FIG. 2: Optical reflection of $\text{Mg}_y\text{Ni}_{1-y}$ as a function of energy and composition. The occurrence of Mg_2Ni is characterized around $y = 0.68$ by a minimum at $\hbar\omega = 1.7$ eV; that of MgNi_2 around $y = 0.3$ by reduced values for most visible photon energies. The irregular transition at $y = 0.60$ is due to a slightly different alignment of samples for $y > 0.60$ and $y < 0.60$.

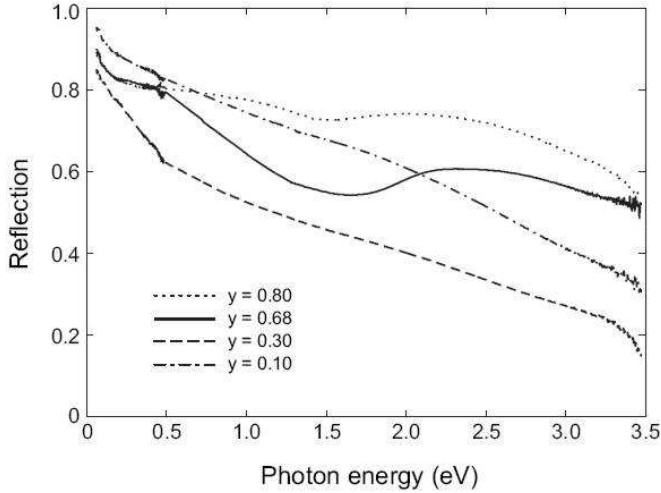


FIG. 3: Optical reflection of $\text{Mg}_y\text{Ni}_{1-y}$ for some selected compositions. Clearly visible are the interband absorption for $y = 0.68$ at $\hbar\omega = 1.7$ eV and the significant lowered screened ω_p for $y = 0.30$.

$\text{Mg}_y\text{Ni}_{1-y}$ compositions in the range $0.07 < y < 0.86$ on glassy carbon substrates (Figs. 2 and 3).

The reflection increases slightly on the addition of Mg and varies at for instance $\hbar\omega = 2$ eV from 75% at $y = 0.86$ to 65% at $y = 0.07$. This can be understood from the fact that only very weak absorption processes are present in alkali metals and alkali earths (like Mg), which have only s electrons in the valence band. They therefore follow the Drude model well, which predicts a high reflection up to the plasma frequency ω_p . On the other hand, between parallel d bands in Ni interband absorption plays a significant role and the reflectivity is lowered before ω_p .

The reflection measurements show two regions of much lower intensity around $y = 0.68$ and 0.3 , which correspond well to the compositions of the stoichiometric alloys Mg_2Ni and MgNi_2 , respectively. However, as can be seen from Fig. 2, both composition regions have different spectral features. Around $y = 0.33$ the screened plasma frequency is significantly lowered for a very broad composition range, which results in a strongly reduced reflection down to infrared energies. Most probably this is caused by various interband absorption processes due to MgNi_2 . The minimum around $y = 0.68$ is different in a sense that it extends over a much smaller energy range. This dip around $\hbar\omega = 1.7$ eV indicates the presence of well-determined interband absorption at this photon energy. The absorption becomes broader and stronger as y approaches 0.68 and forms a very well defined minimum both in energy and composition (cf. Fig. 2). As will be demonstrated in the next sections, the local reflection minimum around $y = 0.68$ is due to the site-ordered Mg_2Ni phase, whereas the minimum around $y = 0.33$ is caused by the structurally disordered MgNi_2 phase.

From the optical reflection, the dielectric function $\varepsilon(\omega) = \varepsilon_1 + i\varepsilon_2$ can be parameterized with a Drude-Lorentz model,

$$\varepsilon(\omega) = \varepsilon_\infty - \frac{\omega_p^2}{\omega^2 + i\omega/\tau} + \sum_{j=1}^N \frac{f_j}{\omega_{0,j}^2 - \omega^2 - i\omega\beta_j}. \quad (1)$$

The free electron conductivity is described by the Drude term with τ the relaxation time, and the effect of interband transitions by the N Lorentz terms with f_j the oscillator strength, $\omega_{0,j}$ the resonance frequency and β_j the broadening. Metallic Mg-Ni reflections can be modelled using the Drude term and only one Lorentz oscillator that accounts for interband transitions. This gives relaxation times for the Mg-Ni system typically in the order of $10^{-14} - 10^{-15}$ s. The real and imaginary part of the dielectric function are plotted in Fig. 4 for some selected compositions. For comparison, the dielectric function of pure metallic Ni from ref. 11 is displayed. On increasing y , ε_1 first increases until $y = 0.4$ and then decreases towards $y = 0.8$. ε_2 shows the opposite behavior, it first decreases until $y = 0.4$ and then increases towards $y = 0.8$. As can be seen from Fig. 4, on decreasing y the experimental $\varepsilon(\omega)$ well approaches the dielectric function of pure Ni.

B. Electrical resistivity

Optical properties showed indications for the formation of the two intermetallic phases Mg_2Ni and MgNi_2 to be present in as-deposited Mg-Ni composition gradient films. However, the arrangement of the atomic components on the crystal lattice, i.e., the degree of which the phases are ordered remains to be specified. This structural property of the film appears to play a role on hydrogenation and will be discussed in this section by means

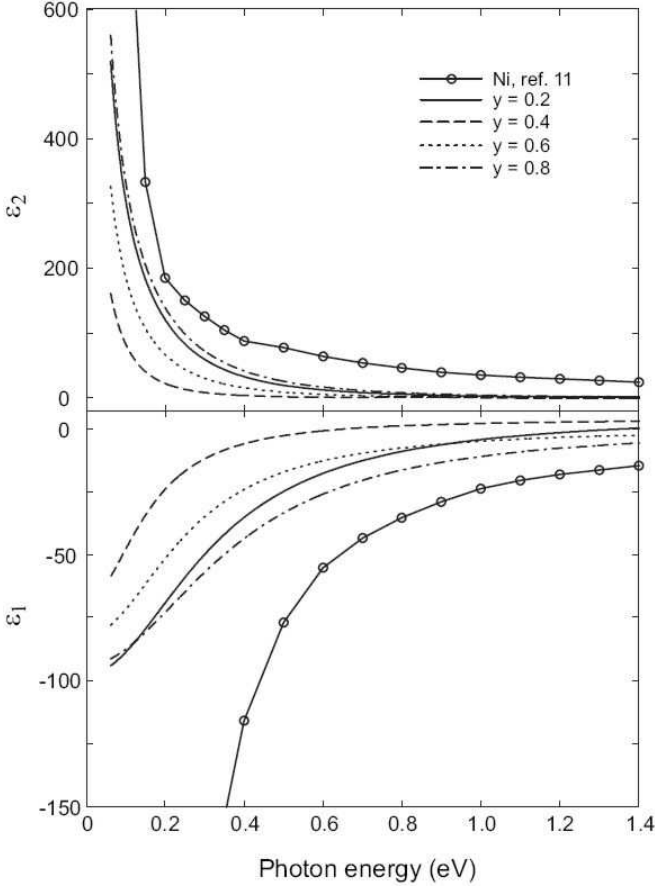


FIG. 4: Real (ϵ_1) and imaginary (ϵ_2) part of the dielectric function obtained from fits to the measured $\text{Mg}_y\text{Ni}_{1-y}$ reflection between $0.062 < \hbar\omega < 3.5$ eV for some selected compositions that are indicated in the legend. For comparison ϵ_1 and ϵ_2 of pure metallic Ni are displayed from ref. 11.

of the electrical resistivity.

DC Resistivity

DC resistivity measurements were carried out for $\text{Mg}_y\text{Ni}_{1-y}$ compositions between $0 \leq y \leq 1$ on glass substrates. Five partially overlapping composition gradient samples were needed to cover this composition range. The experimental electrical resistivity of pure Mg ($y = 1$) and pure Ni ($y = 0$) are 5.69 ± 0.06 and $10.59 \pm 0.09 \mu\Omega\text{cm}$, respectively, which is slightly higher than literature values¹². This is probably due to a thin oxide layer on top of the film, to impurities in the film and/or to structural imperfections due to the deposition technique.

Theoretically, the room temperature electrical resistivity of a concentrated binary metallic alloy system, which consists of a single phase can be described by Nordheim's rule¹³. This predicts the resistivity to be mainly caused by s-s electron transitions, implying the dependence on composition to be parabola-shaped with

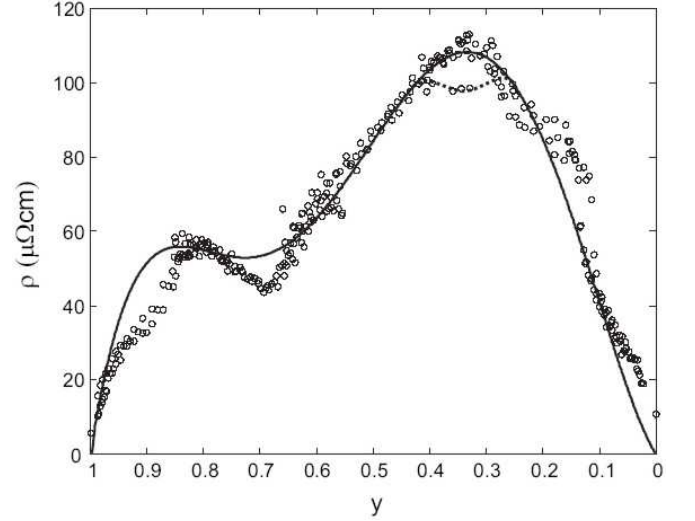


FIG. 5: The composition dependence of the measured room temperature DC resistivity ρ_{DC} of $\text{Mg}_y\text{Ni}_{1-y}$. The solid line displays the fit based on Eq. 2. The dotted line shows a guide to the eye for lowered resistivity values that are occasionally measured around $y = 0.33$.

a maximum around the equiatomic composition. This maximum resistivity indicates a disordered arrangement due to a random mixture of the component atoms. However, solid solution systems involving transition metals like Ni, generally do not obey Nordheim's rule. For these systems also s-d transitions contribute to the total resistivity. In the transition metal poor region, the d band is filled which prevents transitions between the s and d band and therefore the scattering probability is low, which points to low resistivity values. On increasing the transition metal amount, the density of empty states into which an electron can be scattered increases and consequently also the resistivity. The resistivity of such a single phase, totally disordered alloy can be expressed as the sum of the partial resistivities due to s-s and s-d transitions, respectively:

$$\rho_{\text{DC}} = A(1-y)y + B(p-y)^2(1-y)y^2, \quad (2)$$

where $1-y$ is the atomic proportion of the transition metal and A, B and p are constants.¹⁴ Eq. 2 describes a bell-shaped compositional dependence for which the maximum resistivity occurs at a transition metal rich composition.

Fig. 5 shows the experimental room temperature DC resistivity of $\text{Mg}_y\text{Ni}_{1-y}$ together with a fit based on Eq. 2, for which $A = 0.248, B = 6.51$ and $p = 0.665$. For many compositions, the fit curve nicely coincides with the highly reproducible experimental values, both showing the bell-shaped composition dependence with an asymmetrically located maximum of about $108 \mu\Omega\text{cm}$ around $y = 0.33$. As the composition of the MgNi_2 phase is exactly centered around this maximum it indicates this phase to be structurally disordered. Note further the significantly lowered resistivity compared to the fit between

$y = 0.6$ and 0.8 . In several alloys of specific stoichiometric compositions, the unlike atoms can preferentially populate distinct lattice sites creating an ordered arrangement of the atoms on the crystal lattice sites.¹⁵ The ordering processes result in a considerable reduction of the residual resistivity of the alloy. As Eq. 2 only assumes a single phase alloy, deviation of the fit with respect to the experimental values is expected for these compositions. The resistivity dip is centered around the composition of the Mg_2Ni phase, which means that contrary to MgNi_2 , the Mg_2Ni phase has a well-ordered structure.

The maximum around $y = 0.33$ has occasionally also been observed as a resistivity minimum, indicating the formation of ordered MgNi_2 (see Fig. 5). Typically, five identical glass substrates are placed next to each other which are deposited simultaneously. In some cases, only one of the gradient samples had the ordered MgNi_2 feature, whereas neighboring samples showed disordered MgNi_2 . Whereas Mg-Ni gradient samples that are deposited from the elements always show the ordered Mg_2Ni structure, the ordered MgNi_2 phase occurs only occasionally and seems to have a lower probability to be formed at room temperature. Since the resistivity at $y = 0.33$ can occur as a minimum or a maximum, the MgNi_2 composition is suspected to be an order-disorder alloy. Based on systems like e.g. the Mn-Ni, which also possesses an ordered structure MnNi_3 comparable to Mg_2Ni in the Mg-Ni system, the Mg_2Ni composition is probably an order-disorder alloy as well.

Furthermore, large deviations with respect to the fitting curve are present around $y = 0.15$ and 0.9 , pointing phases with a disordered and ordered arrangement, respectively.

Optical Resistivity

In order to check the mutual agreement between the electrical and optical properties, the DC resistivity ρ_{DC} can be compared to the optical resistivity ρ_{opt} that is obtained from the Drude fit parameters of the optical reflection spectra (see section III A). ρ_{opt} is related to the plasma frequency and the relaxation time by

$$\rho_{\text{opt}} = \frac{1}{\varepsilon_0 \omega_p^2 \tau}, \quad (3)$$

where ε_0 is the vacuum permittivity, and is depicted in Fig. 6. Since the infrared part of the reflection spectra for $0.4 \lesssim y \lesssim 0.6$ could not sufficiently well be fitted, the optical resistivity in this range is omitted. Fig. 6 shows the DC resistivity to be in agreement with the optical resistivity. Around $y = 0.33$ ρ_{opt} coincides with ρ_{DC} which indicates that also optical measurements show MgNi_2 to have a structurally disordered appearance on the lattice. Moreover, it implies that the effect of disorder evaluated at $\omega = 0$ and at optical frequencies $\omega \sim 10^{14} - 10^{16} \text{ s}^{-1}$ is comparable. The optical resistivity further shows reduced values around the composition of Mg_2Ni , though

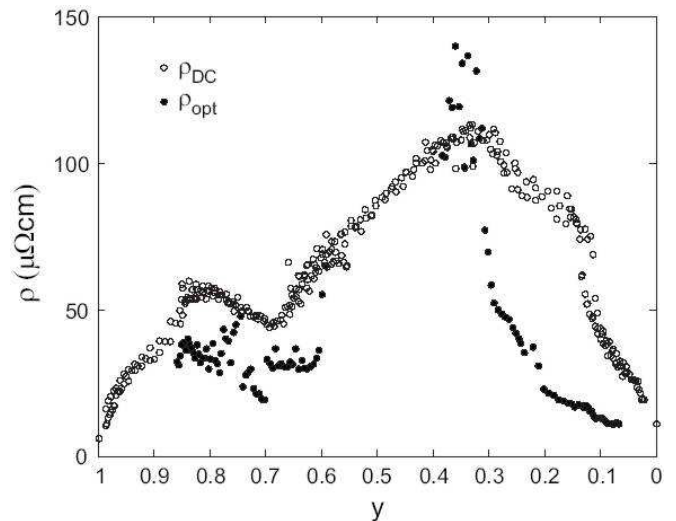


FIG. 6: The composition dependence of the optical resistivity ρ_{opt} of $\text{Mg}_y\text{Ni}_{1-y}$. Since the infrared part of the reflection spectra for $0.4 \lesssim y \lesssim 0.6$ could not sufficiently well be fitted, the optical resistivity of this part is omitted. For comparison, the DC resistivity ρ_{DC} is depicted.

less pronounced than in the DC resistivity curve. Differences between ρ_{opt} and ρ_{DC} may occur in this region where $\omega\tau \gtrsim 1$, i.e., where one period of the oscillating electrical field is of the same order of magnitude as the relaxation time. Both electrical and optical properties are thus in good agreement with respect to the structurally disordered MgNi_2 phase.

C. Structure

In the previous sections, optical and electrical properties showed features of phase formation of Mg_2Ni and MgNi_2 around their corresponding compositions. In this section, X-ray diffraction will establish the presence of Mg_2Ni in Mg-Ni films that are sputter-deposited at room temperature. In the film layer, clusters of crystalline Mg_2Ni form crystallites that are embedded in an amorphous metallic matrix of e.g. Mg_2Ni , Mg and Ni. These structural properties of the film will be discussed for the region where Mg_2Ni can be detected.

X-ray diffraction measurements in the composition range $0.41 < y < 0.83$ indicate the presence of the Mg_2Ni phase through its (003) and (006) reflections (see Fig. 7), which are only observed between $0.58 < y < 0.81$. Apart from Mg_2Ni , no other phases could be detected. Since the width of the (006) reflection is approximately equal for all compositions, rocking curves of this reflection can be mutually compared. They show a remarkable relation between θ at maximum intensity and the composition, as shown in Fig. 8. From the deposition set-up one would expect the crystal axis at a given position on the substrate to be directed to the most influential target seen from that position. On the Mg rich side, more Mg is de-

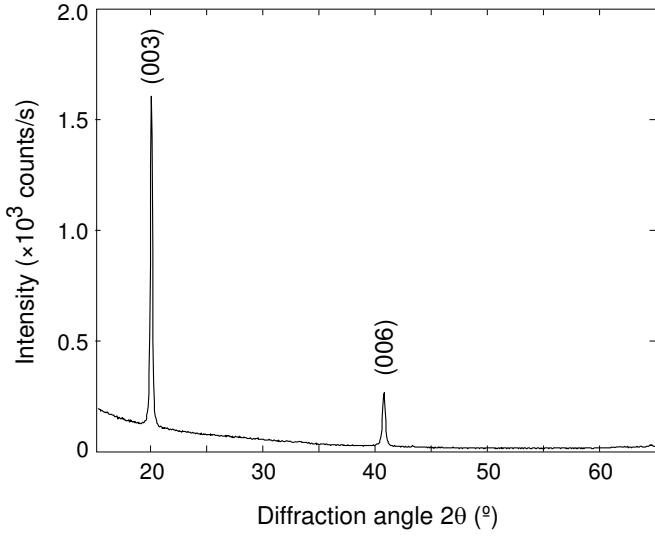


FIG. 7: X-ray diffraction spectrum of as-deposited sputtered $\text{Mg}_y\text{Ni}_{1-y}$ on a Si substrate for $y = 0.68$. The Mg_2Ni (003) and (006) reflections show the c-axis of the hexagonal lattice to be out of plane.

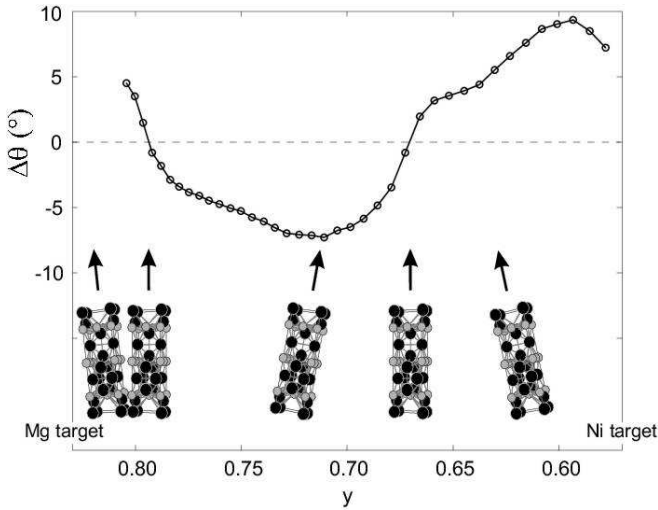


FIG. 8: Composition dependence of the orientation of the c-axis of the Mg_2Ni phase in $\text{Mg}_y\text{Ni}_{1-y}$. $\Delta\theta$ is the deviation of the crystal axis with respect to the perpendicular to the Si substrate, as illustrated for selected compositions by the cartoons of the hexagonal Mg_2Ni unit cell. The location of both sputter targets is indicated.

posited than Ni so the Mg target would be presumed to dominate the deposition process and therefore also the crystal axis direction. For the Mg richest compositions there is indeed a slight tilt $\Delta\theta$ towards the Mg target (which defined as positive). At $y \simeq 0.80$ the c-axis is perpendicular to the substrate and for higher Ni concentrations it points to the Ni target, as would be expected. However, at $y \simeq 0.68$ the c-axis is again perpendicular to the substrate and for $y < 0.68$ it even points towards the Mg target. If one assumes that the particle beams have a

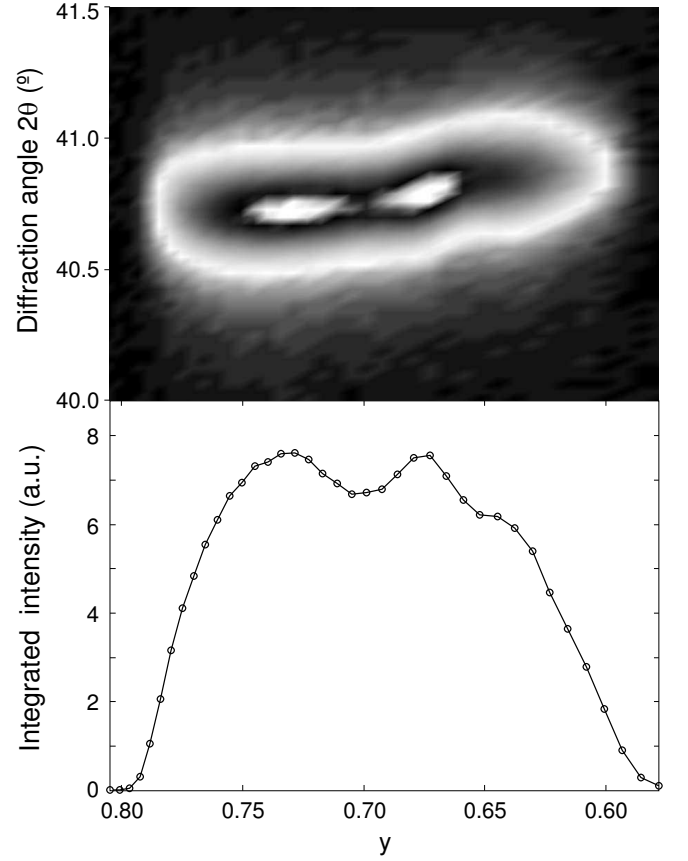


FIG. 9: Upper panel: the Mg_2Ni (006) reflection as a function of composition and diffraction angle 2θ . θ is adjusted for the c-axis direction (cf. Fig. 8). Lower panel: the composition dependence of the integrated (006) reflection, displaying the amount of crystalline Mg_2Ni in $\text{Mg}_y\text{Ni}_{1-y}$.

homogeneous space distribution — which is confirmed by the monotonic composition gradient — at the Ni rich side the Ni target would be expected to have a dominant effect on the crystal orientation. Most probably the crystal axis is not only determined by the mutual particle beam currents but also by particle migration on the film surface. Note, however, also the inexplicable correlation for $y = 0.68$ and 0.80 between the fact that $\Delta\theta = 0$ and the significantly enlarged transmission in the hydrogenated state (cf. Fig. 1b).

Once having the direction of the Mg_2Ni crystal axis, the amount of Mg_2Ni can be determined as a function of composition (Fig. 9). For this purpose, $\theta - 2\theta$ scans are performed for the (003) and (006) reflection with $\theta' = 2\theta/2 + \Delta\theta$, i.e., with θ adjusted for the tilt of the crystal c-axis compared to the (400) reflection of the Si substrate. For angles 2θ which showed a reflection peak due to Mg_2Ni , the amorphous signal has been simulated based on regions with no distinguishable peak, which was then subtracted from total reflection signal. Integration of the peak gives the amount of crystalline Mg_2Ni that can be observed by XRD. As can be seen from Fig. 9,

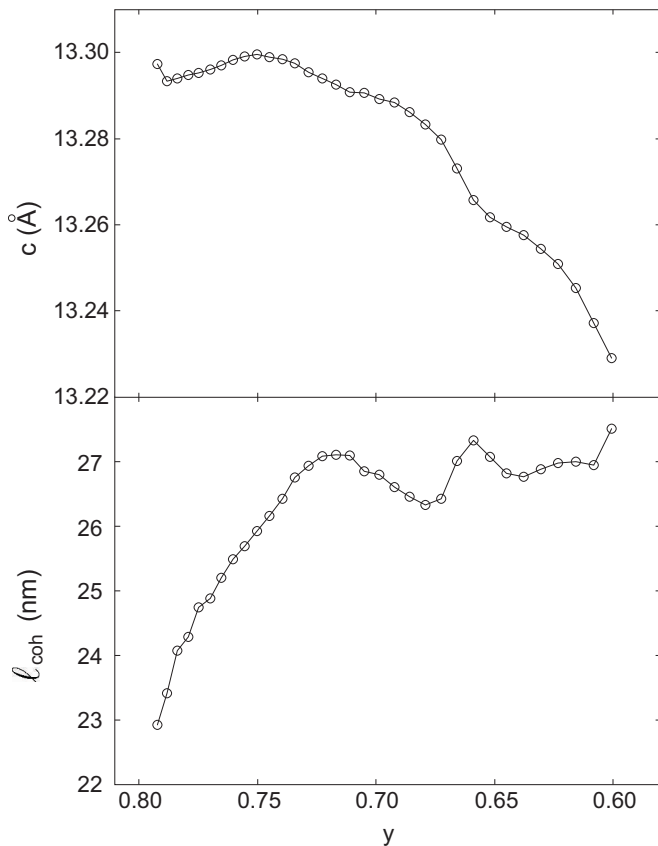


FIG. 10: Upper panel: the composition dependence of the c -axis lattice parameter c of Mg_2Ni in $\text{Mg}_y\text{Ni}_{1-y}$. Lower panel: the composition dependence of the coherence length ℓ_{coh} of Mg_2Ni clusters in $\text{Mg}_y\text{Ni}_{1-y}$.

Mg_2Ni is present for $0.58 < y < 0.81$ though it preferentially forms at Mg rich compositions. Although from the Mg-Ni phase diagram the highest amount of Mg_2Ni is expected at one composition, $y = \frac{2}{3}$, Fig. 9 shows two compositions with an equal maximum amount Mg_2Ni , at $y = 0.68$ and 0.73 . It should also be noticed that only at $y = 0.68$ the total reflection signal is reduced by more than 30%. This means that at this composition there is much less amorphous Mg_2Ni than elsewhere, which makes it relatively the most crystalline composition.

The c -axis lattice parameter can be deduced from the peak position of the Bragg reflection at each composition and is displayed in Fig. 10. The lattice mainly expands from $y = 0.60$ to 0.76 after which it gets smaller to Mg rich compositions. Since the molar volumes of Mg and Ni are 13.98 and 6.59 cm^3 , respectively¹², the expansion can be explained by the increasing amount of Mg next to Mg_2Ni . At compositions where an elevated amount of Mg_2Ni is observed, $y = 0.68$ and 0.73 , the c -axis distribution shows a slightly reduced lattice spacing, here also indicating the presence of a crystalline phase.

A measure of the size of Mg_2Ni grains in the c -direction is given by the coherence length ℓ_{coh} , which should be smaller or equal to the grain size. ℓ_{coh} can be estimated

from the width of the diffraction peak by the Scherrer equation¹⁶,

$$\ell_{\text{coh}} = \frac{K\lambda}{\beta \cos \theta}, \quad (4)$$

where λ is the emitted wavelength, β is the peak width at half maximum (in radians), θ the diffraction angle, and K a factor which depends on the shape supposed for the intensity distribution of diffraction. As a first attempt K is assumed to be 0.9 . Fig. 10 shows the coherence length in the growth direction which increases from the Mg rich part to the Mg poor part from 23 to about 27 nm. Around $y = 0.68$ and 0.73 the coherence length is increased, indicating the formation of larger crystallites. In the film layer, this implies on average an enhanced crystallinity due to Mg_2Ni which supports the observed elevated amount of Mg_2Ni for both compositions.

D. Surface morphology

X-ray diffraction revealed the structure of the as-deposited Mg-Ni thin films in the region that contained crystalline Mg_2Ni . In order to complete the structural picture, in this section we will discuss the surface morphology of as-deposited Mg-Ni films on Al_2O_3 substrates for compositions $0.55 < y < 0.85$.

The surface morphology at some selected compositions is depicted in Fig. 11. The SEM images show a cauliflower-like pattern, except around 0.66 where the surface looks like a field of connected, sharp thorns, suggesting an enhanced surface roughness. AFM, which has a much higher resolution, confirms this behavior. In order to quantify the observed roughness, the root-mean-square (rms) of the height deviations is deduced from AFM measurements and is plotted in Fig. 12. From $y = 0.85$ to 0.78 the roughness linearly decreases from 2.3 nm to 0.6 nm, where the surface is rather flat. A maximum of 4 nm is attained around $y = 0.65 - 0.67$, which is in accordance with the SEM measurements. Below $y = 0.60$ the roughness is less than 0.15 nm, which indicates an almost completely flat surface.

Also from AFM measurements the surface grain size is determined, and is plotted in Fig. 12. Between $y = 0.78$ and 0.85 the mean grain diameter is $35 - 45$ nm, irrespective of composition. Between $y = 0.65$ and 0.74 an elevated grain size is observed of about 60 nm, which decreases sharply for higher Ni contents.

In general, surface morphology can be intrinsic to the structure of the deposited composition, be due to oxidation during deposition, be caused by post-growth surface oxidation or be due to the Pd cap layer. The latter two reasons are possibilities as the films are capped with only 4 nm Pd that form islands instead of a closed layer between which oxidation can occur. In order to trace the origin of the observed morphology, the oxygen content was measured by RBS. At the substrate/film interface and in the film layer no oxygen has been observed

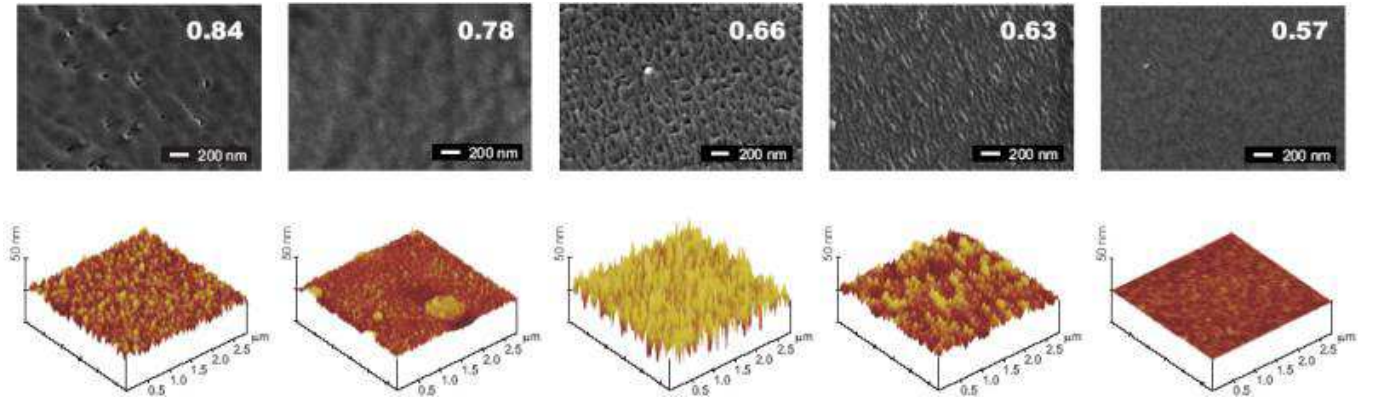


FIG. 11: The surface morphology of $\text{Mg}_y\text{Ni}_{1-y}$ for some selected compositions that are indicated in the right corners of the upper series images. For comparison surfaces recorded by SEM (upper series) and AFM (lower series) are displayed together.

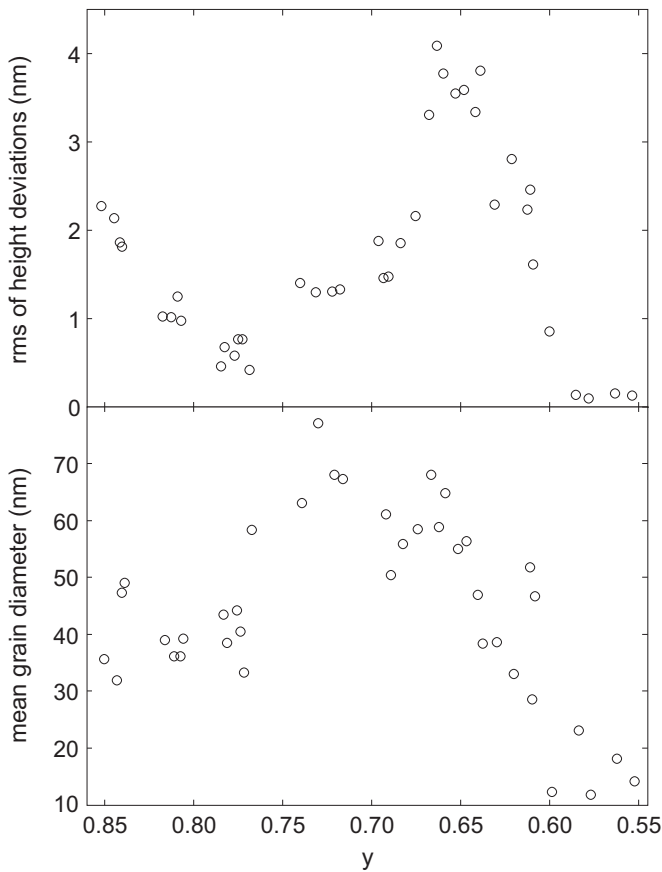


FIG. 12: Upper panel: the root-mean-square (rms) of height deviations at the surface of $\text{Mg}_y\text{Ni}_{1-y}$ plotted versus composition. Lower panel: the composition dependence of the mean surface grain diameter as determined from AFM measurements on $\text{Mg}_y\text{Ni}_{1-y}$ surfaces.

for the investigated range of compositions. At the surface, the oxygen content is completely independent of composition and is on average $1.74 \times 10^{16} \pm 0.92 \times 10^{16}$ atoms/cm². Also the Pd content has been measured by RBS, which turned out to be composition independent

too. One therefore can conclude that the observed composition dependent surface morphology is completely inherent to the structure of the deposited composition.

The roughness and the grain size appear to have the same trend and show elevated values for $0.60 \lesssim y \lesssim 0.75$. Since this range coincides with the composition region for which crystalline Mg_2Ni is observed by XRD (see section III C), Mg_2Ni thus provokes rough surfaces. The kinetics of the hydrogenation process is dependent on the surface roughness, which is therefore expected to be enhanced in the presence of Mg_2Ni .

The structure of cross sections of the film has been investigated by SEM through looking at regions where the film has been broken open, caused by externally applied stresses. Due to the deposition method a columnar structure is observed in the as-deposited state. At the surface each column has a hemispheroidal top that together form the cauliflower structure as seen from above. Therefore, the surface grain size, as discussed earlier, can be considered to be the surface of these hemispheroidal tops.

E. Discussion

In the foregoing sections, as-deposited Mg-Ni composition gradient samples were subject to different techniques in order to quantify the binary Mg-Ni alloy system. Fig. 13 displays the optical, electrical, structural and morphological properties as a graphical summary of the metal system. Optical reflection measurements showed two minima that indicated the formation of the intermetallic alloys Mg_2Ni and MgNi_2 (Fig. 13a). At exactly the same composition ranges, the electrical DC resistivity showed a site-ordered arrangement on the crystal lattice for the phase that was supposed to be Mg_2Ni and a structural disordered arrangement for supposed MgNi_2 (Fig. 13b). The two regions of lowered optical reflection can thus be explained by a site-ordered structure of Mg_2Ni which gives rise to a well-defined interband ab-

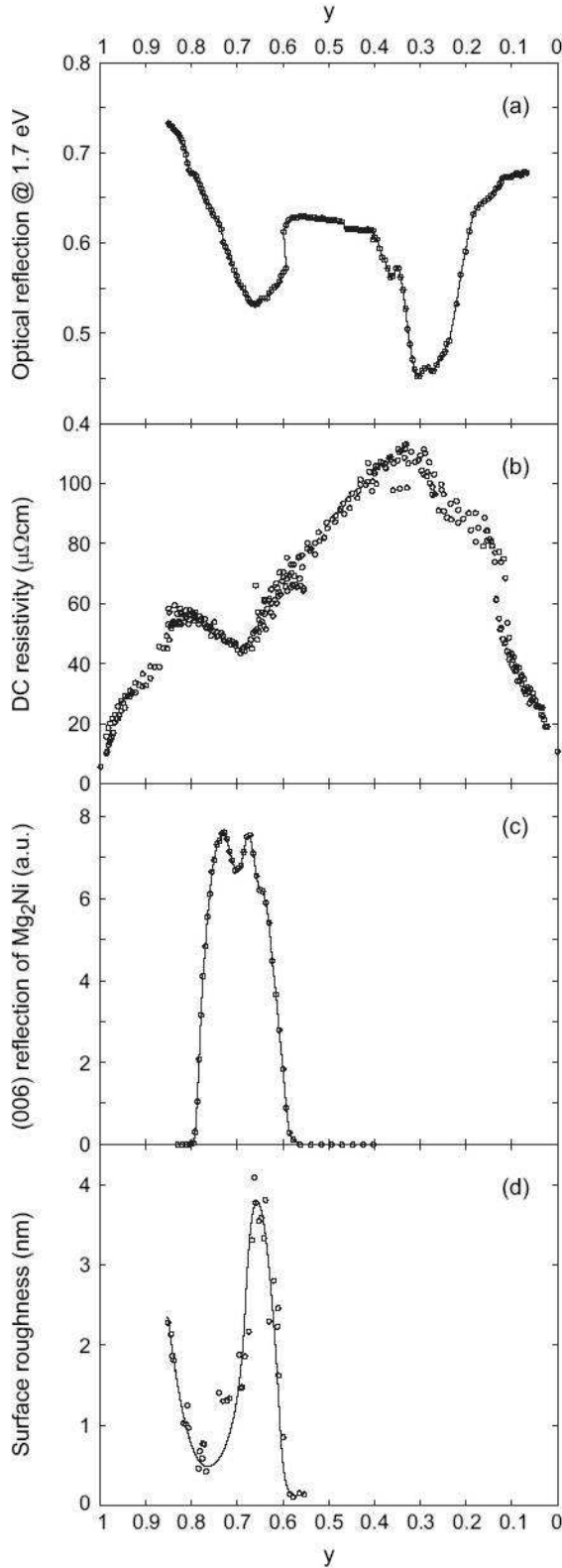


FIG. 13: Summary of the properties of the as-deposited metallic Mg-Ni system. The presence of Mg_2Ni for $0.6 < y < 0.8$ is shown by: (a) the optical reflection, (b) the DC resistivity, (c) the (006) Bragg reflection of Mg_2Ni and (d) the surface roughness displayed by the rms of height differences at the surface. The presence of MgNi_2 around $y = 0.33$ is indicated by the optical reflection and the DC resistivity.

sorption around $\hbar\omega = 1.7$ eV, and by structurally disordered MgNi_2 for which various interband absorption effects cause a strongly screened plasma frequency down to infrared energies. Further, mutual agreement exists between optical and electrical measurements as they both indicate the presence of Mg_2Ni and MgNi_2 and moreover show the latter one to be structurally disordered.

The presence of Mg_2Ni in a well-defined composition range was established by X-ray diffraction (Fig. 13c). This range corresponds exactly to the composition region for which the optical reflection and the DC resistivity showed lowered values, both already suggesting the Mg_2Ni phase. Remarkable is the elevated presence of Mg_2Ni at two compositions, for $y = 0.68$ and 0.73 , instead of the single one at $y = \frac{2}{3}$ that would be expected from the Mg-Ni phase diagram. Further, also the c-axis lattice size and the coherence length of Mg_2Ni showed an enhanced crystal formation at both compositions.

The presence of Mg_2Ni causes the surface of the thin film layer to be much more rough than for neighboring compositions, as can be concluded from SEM and AFM studies (Fig. 13d). Related is the surface grain size which also shows elevated values if Mg_2Ni is present. Both morphological phenomena occur in a composition range that exactly matches with the optical, electrical and structural anomalies of the Mg_2Ni phase (cf. Fig. 13). Apart from these largely correlating aspects, there are also properties of the Mg-Ni composition gradient films that are less well understood. For example, the DC resistivity shows a widely spread out hump around $y = 0.15$ and a wide dip around $y = 0.9$ (see Fig. 5) pointing to an increased structural disorder and site-order, respectively. However, on the basis of the Mg-Ni phase diagram, no special features are expected for both composition regions and no other measurements were performed at these compositions. Furthermore, the c-axis orientation of the Mg_2Ni crystal (see Fig. 8) showed a very remarkable composition dependence, which can not be explained by considering only the mutual power of the Mg and Ni target during the deposition. Most probably also surface migration of the atoms should be regarded and possibly the direction of the crystal axis is determined by the formed phases too.

IV. THE Mg-Ni-H SYSTEM

The previously described metallic Mg-Ni system will now be considered for the same composition gradient films after hydrogenation. The stripe-like pattern that was observed in transmission by a CCD camera (Fig. 1b) is quantified by photometric spectrometry. In order to understand the result, first a geometrical interference origin is considered. Vibrational spectroscopy then demonstrates the presence of Mg_2NiH_4 and its distribution on composition. Optical analysis further indicates the presence of MgH_2 at Mg rich compositions. For the Ni rich region, i.e., for $y < 0.67$, electrical DC resistivity shows,

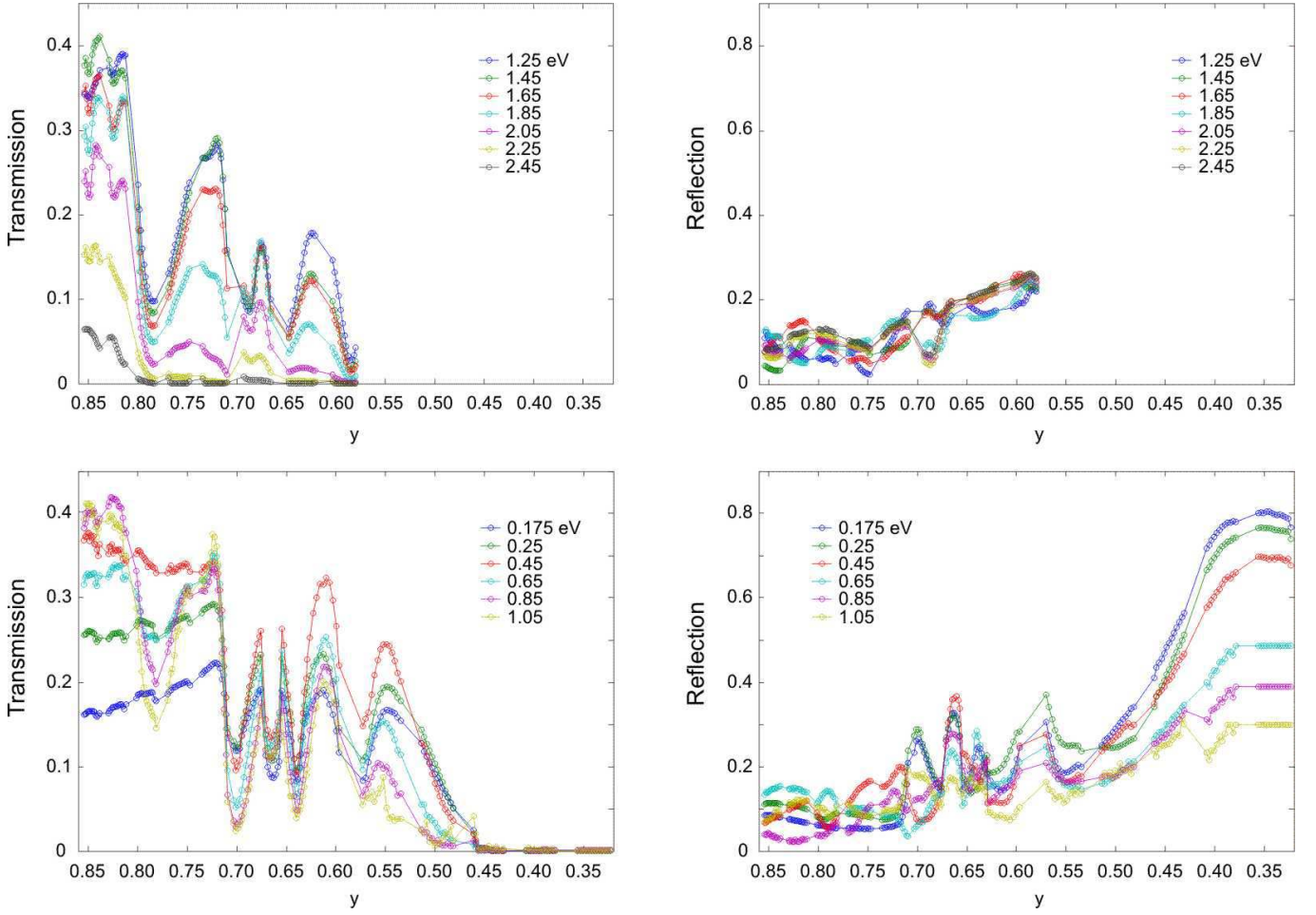


FIG. 14: The composition dependence of the optical transmission and reflection at visible and infrared energies (indicated in the legend) of hydrogenated $\text{Mg}_y\text{Ni}_{1-y}\text{H}_x$ on CaF_2 substrates, covered with a 4 nm thin Pd cap layer.

in a framework of an effective medium theory (Bruggeman approximation) and classical percolation theory, the influence of hydrogen around the equiatomic composition and on the MgNi_2 phase. Eventually, X-ray diffraction measurements are performed to visualize the structure of the hydrogenated Mg-Ni-H thin film.

A. Optical properties

The peculiar optical transmission of the hydrogenated Mg-Ni-H system was illustrated in the *Introduction* by means of a camera recorded image (Fig. 1b). In order to quantify the optical properties, the transmission T and reflection R are measured by photometric spectrometry on composition gradient films ($0.32 < y < 0.86$) on CaF_2 substrates. Fig. 14 shows the very reproducible infrared and visible transmission and reflection spectra for selected photon energies. The visible transmission again displays the composition dependence that was earlier observed as a stripe-like pattern in the camera image. However, for decreasing energies other narrow transmis-

sion maxima appear to develop around $y = 0.65$ and 0.55 . Note the reduced intensity at $y = \frac{2}{3}$ corresponding to the composition of stoichiometric Mg_2NiH_4 . Remarkable is the absence of an enhanced transmission around $y = 0.8$ where the camera image showed a bright yellow stripe. As the spectrometer beam size is about 3 mm and since this region is only 0.5 – 1 mm on the sample, detection seems not to be possible. It should further be pointed out that the optical transmission attains its maximum values at exactly $\hbar\omega = 0.45$ eV for about the entire composition range. Moreover, at the same energy, the composition region around $y = 0.78$ changes from almost composition independent to strongly dependent. Therefore, this energy might be a transition point for different absorbing processes, e.g. polaron absorption below it and interband absorption above it, with minimum absorption effects at 0.45 eV. Eventually, for Ni rich compositions the transmission falls off and is below 0.5% for $y < 0.45$.

The reflection generally shows the mirror image of the transmission, i.e., having a maximum at a transmission minimum. This can be seen by the narrow composition regions which show an enhanced transmission as well as

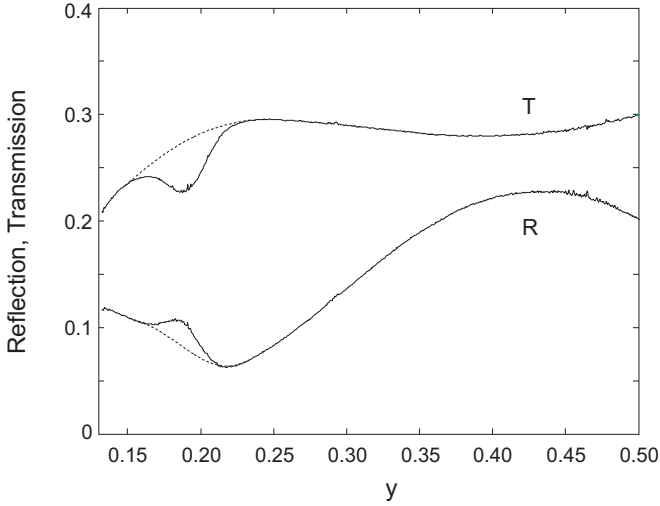


FIG. 15: The optical transmission (T) and reflection (R) at $y = 0.62$ in the hydrogenated state (solid lines). The presence of the $[\text{NiH}_4]^{4-}$ phonon absorption centered around $\hbar\omega = 0.197$ eV has been made clear by plotting the simulated absorption-free signals (dotted lines) as well.

for $y < 0.45$ where the system approaches metallic properties and consequently the reflection increases sharply. However, around $y = 0.78$ the transmission shows a broad dip for $\hbar\omega > 0.45$ eV which is not compensated by an increased reflection, and consequently the absorption $A = 1 - R - T$ is high. This corresponds well to the dark reddish region on the camera image.

It thus appears that Mg-Ni-H composition gradient thin films have a strong composition dependence. However, the ternary Mg-Ni-H phase diagram⁷ only predicts the presence of MgH_2 at Mg rich compositions that gradually changes to Mg_2NiH_4 at Mg poor regions, which can not account for the observed composition dependence. In the following, analysis of the optical properties will lead to an understanding of the transmission pattern.

In general one would expect that a transparent wedge-shaped film where the thickness is of the order of the probing wavelength λ , such as the Mg-Ni-H gradient samples, produces Fizeau fringes when studied in reflection or transmission.¹⁷ Simulation of this interference effect with an overall index of refraction of the Mg-Ni-H layer $n = 3.5$ and an overall absorption coefficient $k = 0.3$ (n and k based on ref. 4 and this work, see Fig. 17), indicates the observed transmission pattern (cf. Fig. 14) not to have an interference origin. In order to be caused by Fizeau interference, the reflection and transmission maxima should move on varying the energy and therefore be separated by a distance $d = \lambda/2\alpha n$, where α is the wedge angle, which increases up to 230 mm for $\lambda = 7.1$ μm (i.e., $\hbar\omega = 0.175$ eV). Since all experimental reflection and transmission maxima are static on varying the energy and separated by unequal distances that are fixed on changing λ , the composition dependence is not due to interference but is intrinsic to the $\text{Mg}_y\text{Ni}_{1-y}\text{H}_x$ layer.

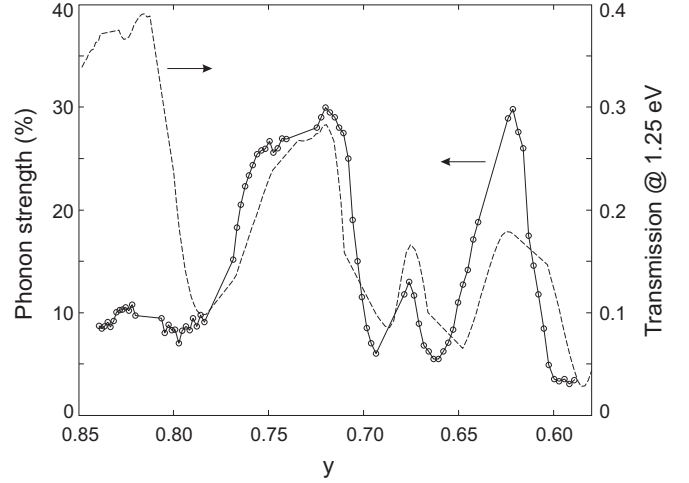


FIG. 16: The composition dependence of the $[\text{NiH}_4]^{4-}$ phonon strength of hydrogenated $\text{Mg}_y\text{Ni}_{1-y}\text{H}_x$. The strength is relative to the absorption-free signal level. For comparison, the optical transmission at $\hbar\omega = 1.25$ eV is shown.

In order to identify the formed species in the $\text{Mg}_y\text{Ni}_{1-y}\text{H}_x$ layer, vibrational spectroscopy is performed in the hydrogenated state. This revealed the presence of Mg_2NiH_4 by the infrared absorption modes of the tetrahedral $[\text{NiH}_4]^{4-}$ cluster. Fig. 15 displays the transmission and reflection spectrum at $y = 0.62$ after hydrogenation. Simulated absorption-free signals are also plotted in order to point out the phonon presence. The phonon absorption is centered around 1585 cm^{-1} (i.e., 197 meV), which is close to literature values^{3,18}, and has a substantial width of $250\text{--}300\text{ cm}^{-1}$ (i.e., 31–37 meV), indicating the Mg_2NiH_4 structure to be polycrystalline.

Fig. 16 depicts the phonon absorption strength for compositions $0.59 < y < 0.84$ which is considered as the height of the absorption compared to the absorption-free signal level. For this purpose, part of the measured spectrum around $\hbar\omega = 0.2$ eV where the absorption takes place has been removed, after which the entire infrared spectrum is fitted in order to obtain the absorption-free signal around 0.2 eV. As can be seen from the figure, for $y < 0.78$ the phonon strength excellently coincides with the optical transmission at $\hbar\omega = 1.25$ eV. This means that for $0.60 < y < 0.78$ the observed transmission is thus mainly due to Mg_2NiH_4 . On the Mg rich side, for $y > 0.78$, the phonon strength is low whereas the transmission is rather high. As Mg_2NiH_4 only slightly participates, in this region another transparent hydride should be formed.

Similar to the optical analysis for the binary metal alloy system (cf. section III A), the optical constants of $\text{Mg}_y\text{Ni}_{1-y}\text{H}_x$ are deduced from the transmission and reflection measurements. A Drude-Lorentz parametrization with 3 Lorentz oscillators is used to describe the complex dielectric function (cf. Eq. 1). The reflection and transmission of the entire layered stack ($\text{CaF}_2 - \text{Mg}_y\text{Ni}_{1-y}\text{H}_x - \text{PdH}_x$) are calculated using a transfer ma-

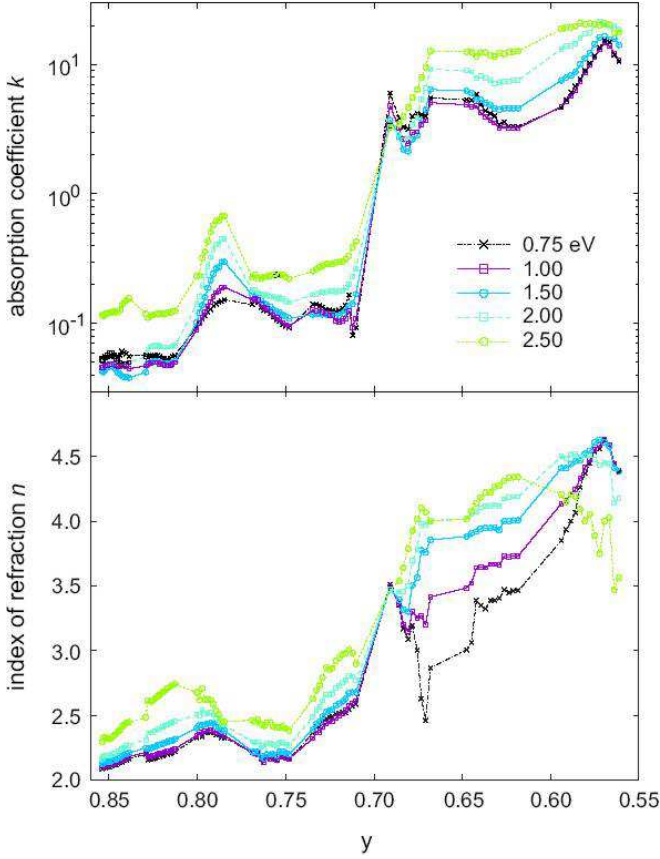


FIG. 17: The composition dependence of the absorption coefficient k and the index of refraction n of $\text{Mg}_y\text{Ni}_{1-y}\text{H}_x$ for some selected photon energies (indicated in the legend).

trix method that considers the Fresnel reflectance and transmittance coefficients at each interface and the absorption in each layer. The fitted ε fulfills the Kramers-Kronig relations and therefore the solution intrinsically satisfies causality. After the fit procedure, comparison of the measured thickness of the metal layer with the thickness fit parameter provides the expansion of the film during hydrogenation. This amounts to an expansion of 36 ± 11 % in case of fitting. Experimentally the expansion has been determined by profilometry on the same sample, which provided a thickness increase of 27 ± 4 %, without showing much composition dependence. Both expansions correspond well to bulk which increases by 32 vol.%⁶.

From the fit parameters the index of refraction n and the absorption coefficient k of $\text{Mg}_y\text{Ni}_{1-y}\text{H}_x$ can be determined by the relationships $\varepsilon_1 = n^2 - k^2$ and $\varepsilon_2 = 2nk$, as plotted in Fig. 17. For $y < 0.8$ it was demonstrated that mainly Mg_2NiH_4 governs the system. In this region n and k have high values of 2.5 – 4.5 and 0.2 – 20, respectively, at $\hbar\omega = 2$ eV. However, for $y \gtrsim 0.7$, the figure shows that n and k drop drastically down. The wide spread region of low optical transmission around $y = 0.78$ is characterized by elevated k values which sup-

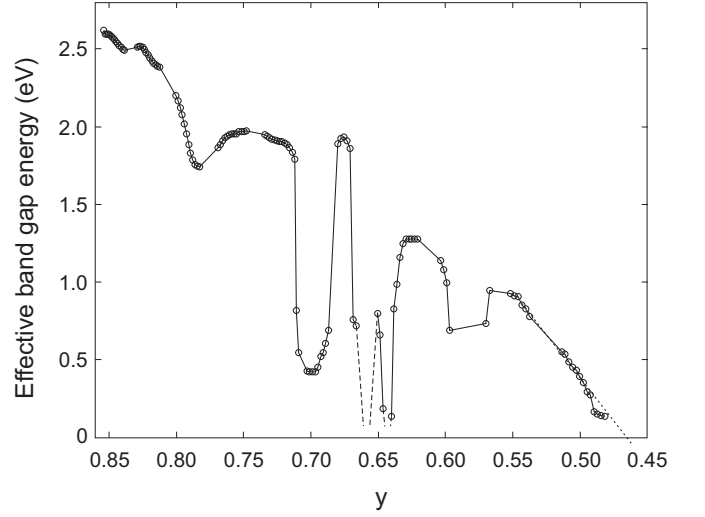


FIG. 18: The composition dependence of the energy of the effective optical band gap E_g , determined from the absorption coefficient α (see text). The dashed lines indicate the behavior of E_g which decreases beyond the measured range. For $y < 0.55$ the band gap energy is fitted by a linear relation (dotted line) which crosses $E_g = 0$ at $y = 0.466$.

port earlier conclusions regarding enhanced absorption. Extrapolation of n and k to $y = 1$ indicates that they approach the literature values of MgH_2 ($n = 1.94 - 1.96$, $k = 7.6 \times 10^{-3}$ at 2.107 eV)^{19,20}. Whereas Mg_2NiH_4 is mainly present for $y < 0.8$ (cf. Fig 16), MgH_2 thus dominates the optical properties for compositions $y > 0.8$. As MgH_2 is a very transparent semiconductor with an optical band gap of 5.6 eV,¹⁹ this fits well to the observed transmission (cf. Figs. 1b and 14).

An effective optical band gap energy E_g of $\text{Mg}_y\text{Ni}_{1-y}\text{H}_x$ can be determined from the energy dependent absorption coefficient α that can be calculated from the transmission T and reflection R by the Lambert-Beer law for an insulating thin layer:

$$\alpha = -\frac{1}{t} \ln \left(\frac{T}{1-R} \right), \quad (5)$$

with t the thickness of the $\text{Mg}_y\text{Ni}_{1-y}\text{H}_x$ layer. The absorption coefficient is typically low below the band gap energy and high above it. Therefore, E_g is determined to be the energy at which α has its maximum increase, which turns out to be between 5×10^4 and 6×10^4 cm⁻¹. Fig. 18 shows also E_g to have a strong composition dependence, which correlates well with the infrared transmission for $\hbar\omega > 0.5$ eV. At the Mg rich part, E_g is large since MgH_2 dominates the system. The effective optical band gap energy at $y = 0.67$, i.e., the composition that is maximally determined by Mg_2NiH_4 , turns out to be 1.95 eV, which is slightly higher than literature values^{21,22}. At the Ni rich part, E_g decreases almost linearly for decreasing y . Extrapolation of E_g to $\hbar\omega = 0$ gives $y = 0.466$ at which the Mg-Ni-H alloy has lost most of its insulating properties. For smaller y the transmission is zero but up

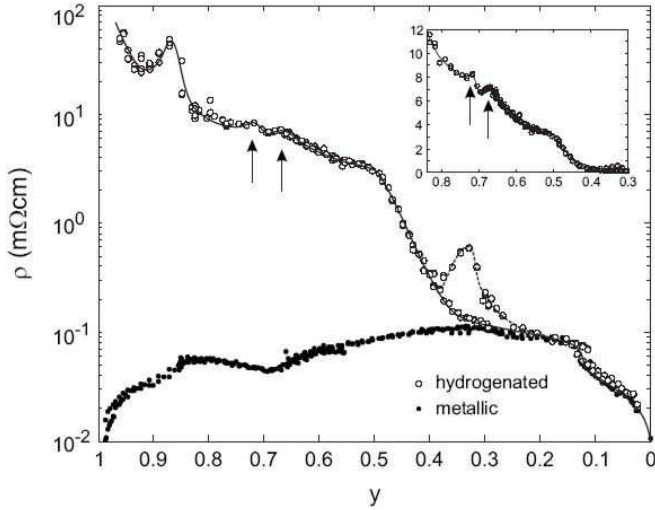


FIG. 19: Composition dependence of the DC resistivity ρ of hydrogenated $\text{Mg}_y\text{Ni}_{1-y}\text{H}_x$ compared to the resistivity of the as-deposited state. Elevated values around $y = 0.67$ and 0.72 are indicated by arrows. Inset: linear plot of the composition dependence of the DC resistivity of hydrogenated $\text{Mg}_y\text{Ni}_{1-y}\text{H}_x$ with emphasis on the maxima at $y = 0.5, 0.67$ and 0.72 . The dotted line shows the enlarged resistivity that is occasionally observed around $y = 0.33$.

to $y = 0.35$ the reflection is still influenced by hydrogen, as can be seen from Fig. 14.

B. Electrical resistivity

In the preceding section, optical analysis elucidated the optical transmission in the Mg rich region ($y > 0.60$) of the Mg-Ni-H system. However, the influence of hydrogen around the equiatomic composition and on the more Ni rich side still remains to be evaluated. There is for instance a substantial infrared transmission around $y = 0.55$ though no Mg_2NiH_4 is present. This section considers the DC resistivity ρ_{DC} of hydrogenated gradient films for compositions $0 \leq y < 0.97$ on glass substrates. In order to demonstrate the influence of hydrogen on compositions around $y = 0.5$ and 0.33 , the measured ρ_{DC} is fitted to an effective medium theory (Bruggeman approximation) and to classical percolation theory.

Fig. 19 displays the DC resistivity of $\text{Mg}_y\text{Ni}_{1-y}\text{H}_x$ before and after hydrogenation. The hydrogenated resistivity starts to deviate from the metallic resistivity for compositions $y \gtrsim 0.2$. Below this value, apparently the presence of hydrogen does not influence the lattice structure. For $y > 0.2$ the hydrogenated resistivity increases, and can be extrapolated up to about $100 \text{ m}\Omega\text{cm}$ at $y = 1$, which fits well to the value of pure MgH_2 . Around $y = 0.68$ the metallic resistivity showed lowered values pointing to the formation of site-ordered Mg_2Ni (section III B). After hydrogenation, two peaks

are present around $y = 0.67$ and 0.72 . In the semiconducting state, an enlarged resistivity indicates the formation of an ordered arrangement on the crystal lattice. These two peaks therefore designate a site-ordered semiconducting phase formation, which correlates with the $[\text{NiH}_4]^{4-}$ phonon strength (cf. Fig. 16) that also showed maximum values for both compositions indicating an enhanced formation of Mg_2NiH_4 . For the Mg rich region, the DC resistivity behavior is thus in agreement with the optical properties.

Around the equiatomic composition the linear representation of the DC resistivity (see inset of Fig. 19) shows a wide-spread hump pointing to increased resistivity values compared to neighboring compositions. Around $y = 0.33$ the hydrogenated system behaves in two ways: most frequently the resistivity gradually drops for decreasing y , however, for about one third of the cases a large hump of $0.60 \text{ m}\Omega\text{cm}$ is measured. Already in the as-deposited case this dual behavior was observed by showing a resistivity maximum and sometimes a minimum (Fig. 5). The lowered resistivity values in the as-deposited state and the increased ones in the hydrogenated state, both point to the presence of a site-ordered phase (see section III B).

Supposed that between $y = 0$ and 0.67 Mg_2NiH_4 is the only (or at least the dominant) insulator and Ni the only metal. Compositions of them then form a composite system of semiconducting Mg_2NiH_4 and metallic Ni. In order to see that the resistivity behavior around $y = 0.5$ and 0.33 can not be described by such a system that in composition changes between a semiconductor and a metal, we will apply two different models to the experimental curves.

For a composite system of semiconducting and metallic clusters, the effective transport properties like the resistivity can be calculated by Bruggeman's effective medium theory^{23,24}. The effective DC resistivity ρ_{DC} of a mixture of Mg_2NiH_4 and Ni is than the solution of the self-consistent relation,

$$(1-x) \frac{\rho_{\text{DC}} - \rho_S}{\rho_{\text{DC}} + A\rho_S} + x \frac{\rho_{\text{DC}} - \rho_M}{\rho_{\text{DC}} + A\rho_M} = 0, \quad (6)$$

where ρ_S and ρ_M are the resistivities of semiconducting Mg_2NiH_4 and metallic Ni, respectively, and x is the metallic volume fraction. The geometric factor A describes the shape of the metallic inclusions in the composite system, and is related to the depolarization factor D through $A = 1/D - 1$. For $D = 1/3$ the inclusions are spherical, whereas $D > 1/3$ and $D < 1/3$ correspond to prolate and oblate spheroids, respectively.²⁵ The vertical axis of rotation of the inclusions are aligned parallel to the c-axis of the metal lattice.

Since Eq. 6 is a monotonic function, it can not describe deviations like the humps we encountered in the resistivity curve around $y = 0.5$ and 0.33 . However, recall that around $y = 0.33$ the system behaves in two ways (see Fig. 19), from which one represents a monotonic change of ρ_{DC} . For the fitting procedure the latter

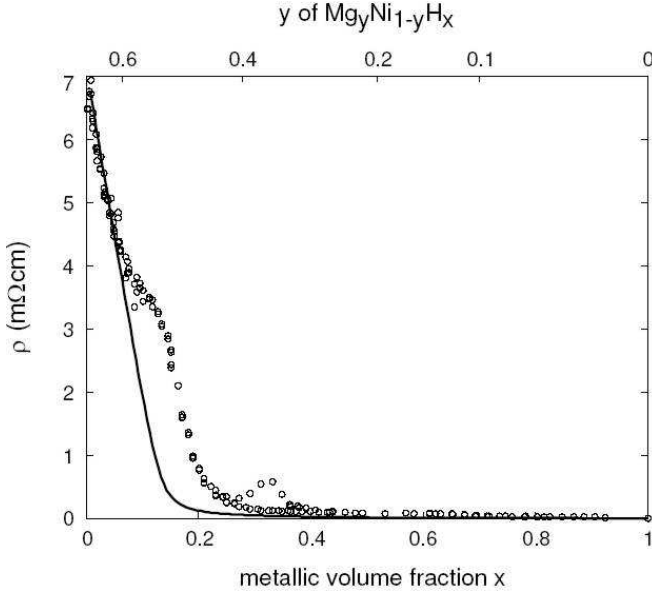


FIG. 20: The electrical resistivity ρ as a function of the metallic volume fraction Ni x in Mg_2NiH_4 . The solid line displays the fit corresponding to Eq. 6.

one is included whereas the region around the equiatomic composition had to be neglected. Fig. 20 shows the measured DC resistivity as a function of the metallic volume fraction Ni together with the fit based on Eq. 6 for a composite Mg_2NiH_4 – Ni system. Here, $\rho_S = 7.11 \text{ m}\Omega\text{cm}$, $\rho_M = 10.59 \text{ }\mu\Omega\text{cm}$, the mass density of Mg_2NiH_4 ²⁶ is $2.706 \times 10^3 \text{ kg/m}^3$ and that of Ni is $8.902 \times 10^3 \text{ kg/m}^3$. The geometrical factor A is easily obtained as a fit parameter, $A = 6.55 \pm 0.12$, which corresponds to a depolarization factor $D = 0.132 \pm 0.002$. The Ni inclusions in the composite mixture are thus oblate spheroids, as also found for the very related $\text{Mg}_2\text{NiH}_{4-\delta}$ – $\text{Mg}_2\text{NiH}_{0.3}$ composite system⁸.

The resistivity behavior around $y = 0.5$ and 0.33 (in case of the hump) can obviously not be described by Bruggeman's effective medium theory which supposes a composite system that gradually changes between a semiconductor and a metal. In order to support the view that in both composition regions different phase formation occurs, classical percolation theory will also be applied to the measured resistivity.

The DC conductivity, $\sigma_{\text{DC}} = 1/\rho_{\text{DC}}$, of a disordered metal-insulator mixture that comprises a network of insulating and metallic clusters can be described by percolation.²⁷ At the percolation threshold x_c a minimum metallic volume fraction generates a continuous conducting network throughout the composite system which causes a steep increase in the conductivity.²⁸ Classical percolation theory then describes the DC conductivity's dependence on the metallic volume fraction x as following a power-law behavior,

$$\sigma_{\text{DC}} \propto (x - x_c)^p. \quad (7)$$

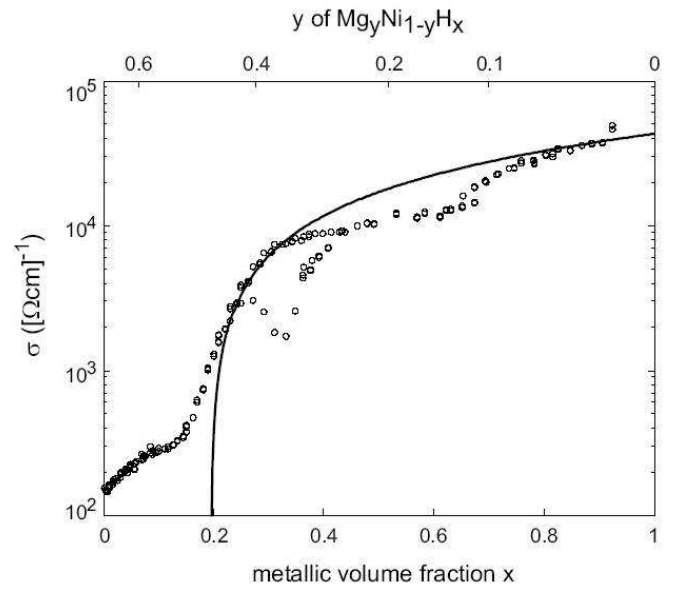


FIG. 21: The electrical conductivity σ as a function of the metallic volume fraction Ni x in Mg_2NiH_4 . The solid line displays the fit corresponding to Eq. 7.

Similar to Bruggeman's effective medium model, Eq. 7 is a monotonic function of x and can therefore not describe local resistivity maxima (and thus conductivity minima) like the ones around $y = 0.5$ and 0.33 . Therefore, in the fitting procedure the monotonically changing resistivity around $y = 0.33$ is included, whereas the region around the equiatomic composition had to be omitted. Fig. 21 shows the measured electrical conductivity of the Mg_2NiH_4 – Ni composite system versus the metallic volume fraction and the fit based on Eq. 7. It should be noticed that due to an irregularity of σ_{DC} around $x = 0.66$ — which is already present in the as-deposited state — the fit does not coincide with measured DC conductivity over the entire composition region. The percolation threshold x_c is 0.195 ± 0.005 (i.e., $0.443 \pm 0.005 \text{ at.\% Mg}$) and the critical exponent p is 0.96 ± 0.02 . Site percolation in an FCC lattice yields $x_c = 0.198$ which is in excellent agreement with the obtained fit parameter. Further, the percolation threshold at $y = 0.443 \pm 0.005$ corresponds very well to the composition at which the effective optical band gap E_g equals zero, i.e., $y = 0.466$ (cf. section IV A), which both describe the onset of metal behavior. The percolation critical exponent in 3D, p , is generally believed to be between 1 and 2.^{27,28,29} The experimentally obtained fit parameter p is very close to 1, which is predicted by effective-medium theory.²⁷

Both Bruggeman's effective medium theory and classical percolation theory described well the overall DC resistivity behavior apart from the two regions (around $y = 0.33$ and 0.5) that showed an unexpected increase of resistivity after hydrogen loading. This means that the behavior of both regions can not be described by a system composed of a binary mixture of Mg_2NiH_4 and Ni.

Nevertheless, hydride phase formation around $y = 0.33$ is suspected since similar to the hydride forming composition $y = 0.67$, the resistivity in the as-deposited and hydrogenated case is lowered and increased, respectively. Moreover, around $y = 0.55$ a substantial infrared transmission is present. For $y < 0.60$, the $[\text{NiH}_4]^{4-}$ phonon strength is very low, which means that almost no Mg_2NiH_4 is formed. Furthermore, the presence of MgH_2 especially at both compositions is very unlikely. Concerning the equiatomic composition, in the metallic state, Orimo and Fujii³⁰ observed amorphous MgNi in bulk by X-ray diffraction, which on exposure to hydrogen becomes hydrogenated as demonstrated by electrochemical measurements. Based on the just mentioned reasons, most likely Mg-Ni-H composition gradient samples contain hydrogenated MgNiH_x around $y = 0.5$. Furthermore, optical measurements are performed down to $y = 0.32$, without showing any transmission for $y < 0.4$. Therefore the increased resistivity around $y = 0.33$ is either due to a non-transparent hydride, most possibly MgNi_2H_x , or to a solid solution of hydrogen in MgNi_2 .

C. Structure

Optical and electrical properties previously showed the distribution of Mg_2NiH_4 , the presence of MgH_2 and hydride formation around $y = 0.5$ and 0.33 in Mg-Ni-H composition gradient thin films. This section considers X-ray diffraction on hydrogenated gradient samples on Si substrates in order to complete the structural picture of the Mg-Ni-H system.

On exposure to hydrogen of an as-deposited Mg-Ni gradient thin film, the (003) and (006) reflection of Mg_2Ni shift to lower diffraction angles, which indicates the formation of the solid solution phase $\text{Mg}_2\text{NiH}_{0.3}$. If hydrogen uptake proceeds, the intensity of both reflections decreases to almost zero, as also seen for $\text{Mg}_y\text{Ni}_{1-y}\text{H}_x$ thin films with $y = 0.67$,³¹ and no other reflection appears. Even for hydrogen loading at pressures up to 10^6 Pa and temperatures of 100°C no reflection of Mg_2NiH_4 and/or MgH_2 has been observed. Although, evidence for hydrogenation was obtained by the presence of optical transmission. The absence of any reflection cannot be caused by the degree of crystallinity as vibrational spectroscopy revealed strong phonon absorptions, but is rather due to the crystal size which might be below the XRD detection limit. Nevertheless, high resolution line scans over the investigated compositions in the hydrogenated state revealed two tiny reflections of the solid solution phase $\text{Mg}_2\text{NiH}_{0.3}$, that mainly exist between $0.74 < y < 0.79$. The presence of $\text{Mg}_2\text{NiH}_{0.3}$ indicates poor hydrogenation for this composition range.

From $\theta - 2\theta$ scans in which θ is adjusted for the orientation of the crystal c-axis, the amount of $\text{Mg}_2\text{NiH}_{0.3}$ can be determined as a function of the deposited composition. The intensity distributions of the (003) and (006) reflection show a maximum around $y = 0.78$, as

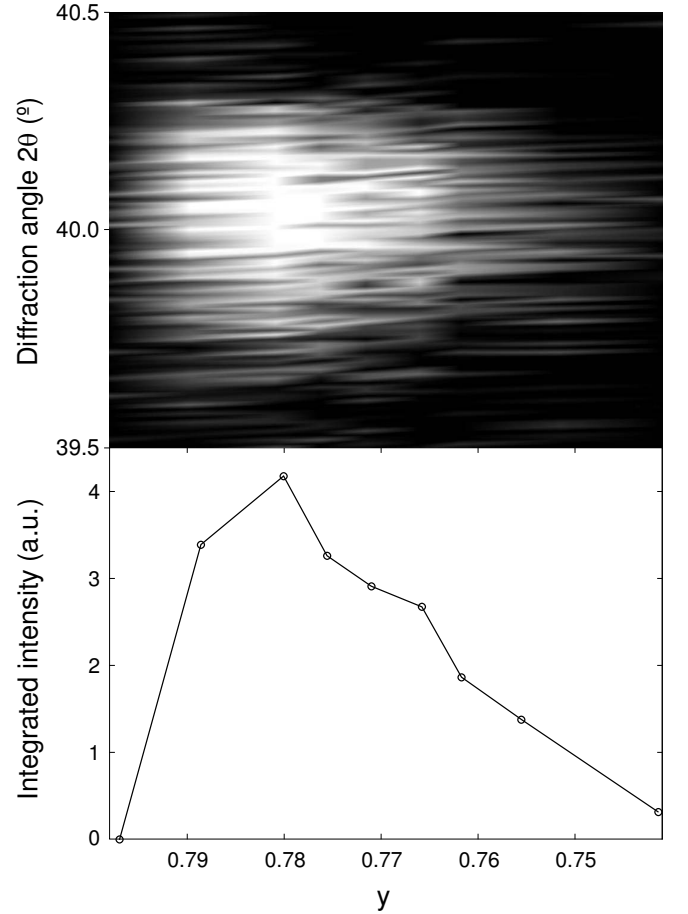


FIG. 22: Upper panel: the presence of the metal solid solution $\text{Mg}_2\text{NiH}_{0.3}$ (006) reflection in hydrogenated $\text{Mg}_y\text{Ni}_{1-y}\text{H}_x$. Lower panel: the composition dependence of the integrated (006) reflection displaying the amount of $\text{Mg}_2\text{NiH}_{0.3}$, which is maximum at $y = 0.78$.

displayed in Fig. 22. Apparently, $y \simeq 0.78$ has the poorest hydrogenation of the entire investigated composition range. This agrees with earlier conclusions based on the optical transmission and reflection and on the absorption coefficient k . As the hydrogen uptake in the film is always hampered by a smooth surface, the AFM observed flatness in the as-deposited state at this composition might be the reason of poor hydrogen loading.

D. Discussion

In the preceding sections, optical, electrical and structural properties of hydrogenated Mg-Ni-H composition gradient thin films showed strong mutual correlations between different probes. This enabled the understanding of the highly composition dependent transmission behavior which does not fit with the predicted Mg-Ni-H phase diagram (see Fig. 1). Fig. 23 shows a graphical summary of the physical properties of the Mg-Ni-H system. Transmission spectra recorded by photometric spectroscopy at

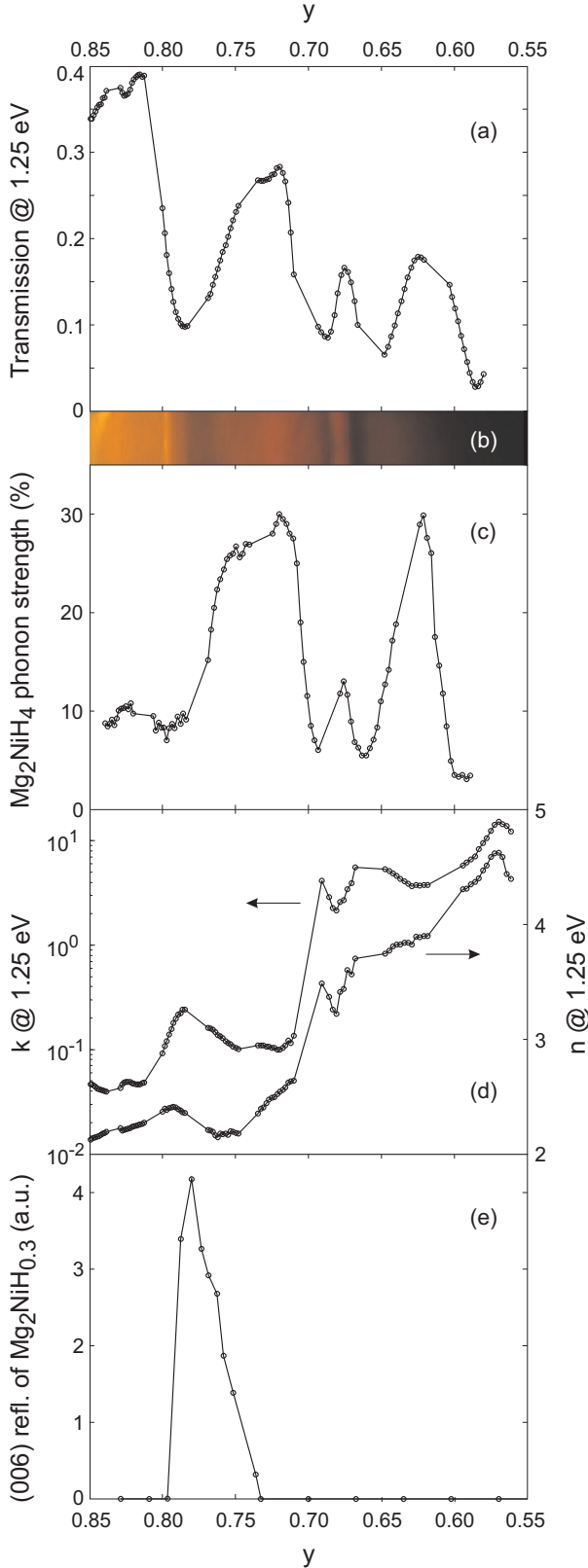


FIG. 23: Summary of the properties of the Mg rich part of the hydrogenated Mg-Ni system. (a) the optical transmission, (b) the optical transmission recorded by a CCD camera, (c) the strength of the Mg_2NiH_4 phonon, (d) n and k at $\hbar\omega = 1.25$ eV and (e) the integrated (006) reflection of $\text{Mg}_2\text{NiH}_{0.3}$.

visible energies (Fig. 23a) perfectly match with the transmission pattern of the camera recorded image (Fig. 23b). The elevated transmission at $y = 0.80$, however, which has a bright yellow appearance in the camera image, could be not probed due to its limited size on the sample. Extra optical contrast is revealed by photometric spectroscopy in the infrared. Vibrational spectroscopy shows the distribution of Mg_2NiH_4 as a function of composition (Fig. 23c) that excellently coincides with the optical transmission in the visible range. The observed transmission between $0.60 < y < 0.8$ is thus due to Mg_2NiH_4 .

For compositions $y > 0.8$ the optical transmission and the optical band gap energy are large, whereas the $[\text{NiH}_4]^{4-}$ phonon strength is low. However, in the same region, the index of refraction n and the absorption coefficient k , that are deduced from the optical transmission and reflection spectra, approach the literature values of MgH_2 (Fig. 23d). Since MgH_2 is a very transparent large band gap semiconductor¹⁹, it can be stated that above $y = 0.8$ MgH_2 dominates the Mg-Ni-H system.

Eventually, around the equiatomic composition and at the more Ni rich region, i.e., for $y < 0.60$, the electrical DC resistivity showed elevated values around $y = 0.5$ and 0.33 that could not fit within a composite system of semiconducting Mg_2NiH_4 and metallic Ni. For $y = 0.5$, this latter phenomenon together with lowered resistivity values in the as-deposited state and a substantial infrared transmission in the hydrogenated state, points to the formation of hydrogenated MgNiH_x . For $y = 0.33$, however, no transmission has been observed. Therefore, either a non-transparent hydride MgNi_2H_x or a solid solution of hydrogen in the intermetallic MgNi_2 phase is formed.

The stripe-like pattern that was shown by the camera recorded image can thus almost completely be understood from the above mentioned properties. Although, the region around $y = 0.78$, where the camera image showed a dark reddish brown region does need some extra attention. The optical transmission and reflection spectra first showed that the absorption $A = 1 - R - T$ in especially this region is high. The absorption coefficient k displayed elevated values pointing to the same conclusion. Eventually, X-ray diffraction measurements in the hydrogenated state indicated an increased amount of the metallic solid solution $\text{Mg}_2\text{NiH}_{0.3}$ only around this composition (Fig. 23e). The high absorption is thus caused by poor hydrogenation, which gives rise to the dark reddish brown appearance. It should be noticed that this region is exactly present in the composition range where the system changes between MgH_2 and Mg_2NiH_4 , i.e., around $y = 0.78$. Most probably the poor hydrogenation is due to the flat surface in the as-deposited state (cf. Fig. 12) which generally slows down the hydrogen uptake.

The colors of the stripe-like pattern, shown in the CCD camera image, correspond well to the effective optical band gap energy E_g . On increasing y the hydrogenated film mainly changes from black to reddish towards yellowish which is also displayed by E_g that in-

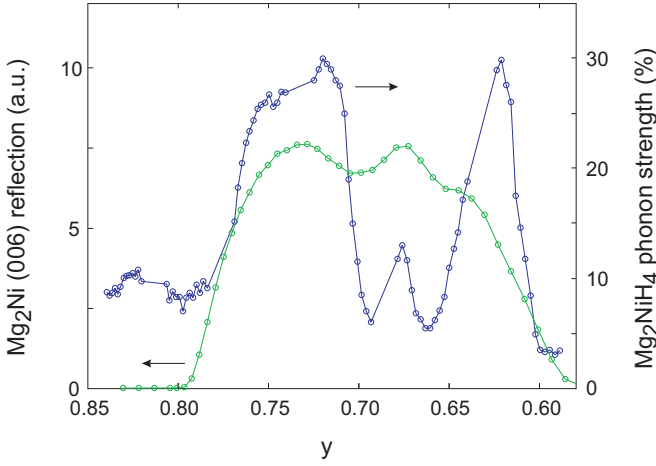


FIG. 24: The presence of Mg_2Ni shown by the total Mg_2Ni (006) reflection and the Mg_2NiH_4 amount expressed by the Mg_2NiH_4 phonon strength. The resembling curves indicate the formation of Mg_2NiH_4 preferentially from Mg_2Ni .

creases from 1 eV at $y = 0.55$ (black visual appearance) to 2 eV at $y = 0.67$ (red) to 2.5 eV (yellow) around $y = 0.85$. The narrow dark regions in between correspond to effective band gap energies in the infrared range (see Fig. 18). As also displayed by $E_g(y)$, the region around $y = 0.65$ has a very low effective band gap energy compared to neighboring compositions and therefore only appears when probed with infrared energies. Remarkable is the $[\text{NiH}_4]^{4-}$ phonon strength which is low at this composition. Therefore, further investigation is necessary to understand the origin of an enhanced transmission at $y = 0.65$.

In the *Discussion* of the metallic Mg-Ni system (section III E), we mentioned the inexplicable lowered electrical resistivity around $y = 0.9$. The DC resistivity in the hydrogenated state (see Fig. 19) shows a huge maximum around the same composition. Similar to composition regions around $y = 0.33$ and 0.67 this points to the formation of a hydride phase. Unfortunately, no optical measurements were performed in this composition range, and further research is necessary to unravel the origin of the behavior around $y = 0.9$.

The relationship between metallic $\text{Mg}_y\text{Ni}_{1-y}$ and hydrogenated $\text{Mg}_y\text{NiH}_{1-y}\text{H}_x$ is given in Fig. 24 which represents the occurrence of Mg_2Ni and Mg_2NiH_4 , respectively. The Mg_2Ni (006) Bragg reflection shows that Mg_2Ni is mainly present between $0.6 < y < 0.8$. After hydrogenation, the phonon absorption strength indicates that Mg_2NiH_4 is exactly present in the same composition range. Moreover, the two compositions with a maximum amount of Mg_2Ni are after hydrogenation transformed into regions that consist of an elevated amount of Mg_2NiH_4 . This means that Mg_2NiH_4 preferentially forms from the crystalline Mg_2Ni phase, instead of being formed from the elements.

V. CONCLUSIONS

The behavior of the Mg-Ni-H system was studied by means of $\text{Mg}_y\text{Ni}_{1-y}\text{H}_x$ composition gradient thin films. In the hydrogenated state, the optical transmission shows a stripe-like pattern of alternating regions of low and high transmission pointing towards a high composition dependence. This phenomenon is all the more unexpected as the predicted Mg-Ni-H phase diagram only represents a gradual change between two transparent hydrides, Mg_2NiH_4 and MgH_2 .

In order to understand the peculiar transmission pattern, first as-deposited metallic Mg-Ni thin films were investigated. The optical reflection in the range $0.062 < \hbar\omega < 3.5$ eV indicated the formation of the intermetallic phases Mg_2Ni and MgNi_2 in well-defined composition regions. The electrical DC resistivity behavior showed both phases to have a site-ordered arrangement and structural disordered arrangement on the crystal lattice, respectively. X-ray diffraction actually established the presence of Mg_2Ni and also showed a maximum occurrence at two compositions instead of solely at $y = \frac{2}{3}$, as would be expected from the binary Mg-Ni phase diagram.

In the hydrogenated state, vibrational spectroscopy showed the presence of Mg_2NiH_4 by the $[\text{NiH}_4]^{4-}$ absorption modes around $\hbar\omega = 0.197$ eV. Its distribution as a function of composition indicates the observed transmission between $0.60 < y < 0.8$ to be completely due to Mg_2NiH_4 . For Mg rich compositions, i.e., $y > 0.8$ optical analysis shows the system to have a strong MgH_2 character. Eventually, around the equiatomic composition and for the more Ni rich region, i.e., $y < 0.60$, the behavior of the electrical DC resistivity points to hydride formation around $y = 0.5$ and 0.33 .

The stripe-like pattern that is observed in transmission at visible energies correlates well to many other physical properties and turns out to be due to a very particular distribution of Mg_2NiH_4 together with the presence of MgH_2 in the Mg rich region.

VI. ACKNOWLEDGEMENTS

The work that is considered in this Master's thesis, has been performed in the Condensed Matter Physics group of Prof. R.P. Griessen at the Vrije Universiteit Amsterdam, The Netherlands (2004). This experimental Master's project has been performed with the help of many persons. First I would like to thank my father, L.F.M.P. van Mechelen, who constructed the electrical resistivity apparatus. Second, but just as valuable, R. Gremaud who assisted during a lot of measurements and with whom discussions helped the interpretation of the measurements. Further, W.J. Lustenhouwer for the WDS composition measurements, S.M. Kars for the SEM measurements, H. Schreuders and D.M. Borsa for the growth of the samples, J.H. Rector for performing RBS measurements, and N.P. Armitage for proofreading the

manuscript. Financial support from the Dutch Stichting voor Fundamenteel Onderzoek der Materie (FOM)

and the Stichting Technische Wetenschappen (STW) is acknowledged.

-
- * Present address: Département de Physique de la Matière Condensée, University of Geneva, Quai Ernest-Ansermet 24, 1211 Genève, Switzerland.
Email : Dook.vanMechelen@physics.unige.ch
- ¹ J.N. Huiberts, R. Griessen, J.H. Rector, R.J. Wijngaarden, J.P. Dekker, D.G. de Groot, and N.J. Koeman, *Nature* (London) **380**, 231 (1996).
 - ² P. van der Sluis, M. Ouwerkerk, and P.A. Duine, *Appl. Phys. Lett.* **70**, 3356 (1997).
 - ³ T.J. Richardson, J.L. Slack, R.D. Armitage, R. Kostecki, B. Farangis, and M.D. Rubin, *Appl. Phys. Lett.* **78**, 3047 (2001).
 - ⁴ J.L.M. van Mechelen, B. Noheda, W. Lohstroh, R.J. Westerwaal, J.H. Rector, B. Dam, and R. Griessen, *Appl. Phys. Lett.* **84**, 3651 (2004).
 - ⁵ P. Nash (Eds.), *Phase Diagrams of Binary Nickel Alloys* (ASM International, 1991).
 - ⁶ J. Schefer, P. Fischer, W. Hälgl, F. Stucki, L. Schlapbach, J.J. Didisheim, K. Yvon, and A.F. Andresen, *J. Less-Common Met.* **74**, 65 (1980).
 - ⁷ K. Zeng, T. Klassen, W. Oelerich, R. Bormann, *J. Alloys Comp.* **283**, 213 (1999).
 - ⁸ S. Enache, W. Loshtroh and R. Griessen, *Phys. Rev. B* **69**, 115326 (2004).
 - ⁹ J.J. Reilly and R.H. Wiswall, *Inorg. Chem.* **7**, 2254 (1968).
 - ¹⁰ L.J. van der Pauw, *Philips Res. Rep.* **13**, 1 (1958).
 - ¹¹ D.W. Lynch, R. Rosei, and J.H. Weaver, *Solid State Commun.*, **9**, 2195 (1971).
 - ¹² D.R. Lide (Eds.), *Handbook of Chemistry and Physics* (CRC Press UK, London, 2005).
 - ¹³ L. Nordheim, *Ann. Phys.* **9**, 641 (1931).
 - ¹⁴ N.F. Mott and H. Jones, *The theory and the properties of metals and alloys* (Dover Publications Inc, New York, 1958).
 - ¹⁵ K. Schröder (Eds.), *Handbook of Electrical Resistivities of Binary Metallic Alloys* (CRC Press Inc., Florida, 1983).
 - ¹⁶ P. Scherrer, *Gött. Nachrichten* **2**, 98 (1918).
 - ¹⁷ see e.g. E. Hecht, *Optics* (Addison Wesley, Inc., 1987).
 - ¹⁸ N. Huang, H. Yamauchi, J. Wu, and Q. Wang, *Z. Phys. Chem. (Munich)* **163**, 225 (1989).
 - ¹⁹ J. Isidorsson, I.A.M.E. Giebels, H. Arwin and R. Griessen, *Phys. Rev. B* **68**, 115112 (2003).
 - ²⁰ F.H. Ellinger, J.C.E. Holley, B.B. McInteer, D. Pavone, R.M. Potter, E. Staritzky, and W.H. Zachariasen, *J. Am. Chem. Soc.* **77**, 2647 (1955).
 - ²¹ W.R. Myers, L.-W. Wang, T.J. Richardson and M.D. Rubin, *J. Appl. Phys.* **91**, 4879 (2002).
 - ²² D. Lupu, R. Sârbu, and A. Biris, *Int. J. Hydrogen Energy* **12**, 425 (1987).
 - ²³ D.A.G. Bruggeman, *Ann. Phys. (Leipzig)* **24**, 636 (1935).
 - ²⁴ R. Landauer, *J. Appl. Phys.* **23**, 779 (1952).
 - ²⁵ L.D. Landau and E.M. Lifschitz, *Electrodynamics of Continuous Media* (Pergamon Press, Oxford, 1984).
 - ²⁶ The molecular volume is deduced from the experimental lattice parameter $a = 6.49$ Å of the Mg_2NiH_4 high temperature phase from ref. 6.
 - ²⁷ B. Abeles, H.L. Pinch, and J.I. Gittleman, *Phys. Rev. Lett.* **35**, 247 (1975).
 - ²⁸ D. Stauffer and A. Aharony, *Introduction to Percolation Theory* (Taylor and Francis, London, 1994).
 - ²⁹ S. Kirkpatrick, *Rev. Mod. Phys.* **45**, 574 (1973).
 - ³⁰ S. Orimo and H. Fujii, *Appl. Phys. A* **78**, 167 (2001).
 - ³¹ W. Lohstroh, R.J. Westerwaal, J.L.M. van Mechelen, C. Chacon, E. Johansson, B. Dam, and R. Griessen, *Phys. Rev. B* **70**, 165411 (2004).